

## A diffusive equilibrium model for the plasma density in Saturn's magnetosphere

A. M. Persoon,<sup>1</sup> D. A. Gurnett,<sup>1</sup> O. Santolík,<sup>2,3</sup> W. S. Kurth,<sup>1</sup> J. B. Faden,<sup>1</sup> J. B. Groene,<sup>1</sup> G. R. Lewis,<sup>4</sup> A. J. Coates,<sup>4</sup> R. J. Wilson,<sup>5</sup> R. L. Tokar,<sup>5</sup> J.-E. Wahlund,<sup>6</sup> and M. Moncuquet<sup>7</sup>

Received 11 November 2008; revised 13 January 2009; accepted 27 January 2009; published 28 April 2009.

[1] Electron density measurements have been obtained by the Cassini Radio and Plasma Wave Science (RPWS) instrument for more than 50 passes through Saturn's inner magnetosphere from 30 June 2004 to 30 September 2007. The electron densities are derived from RPWS measurements of the upper hybrid resonance frequency and span latitudes up to 35° and  $L$  values from 3.6 to 10. The electron density measurements are combined with ion anisotropy measurements from the Cassini Plasma Spectrometer (CAPS) and electron temperature measurements from the RPWS and CAPS to develop a diffusive equilibrium model for the distribution of water group ions, hydrogen ions, and electrons in the inner region of Saturn's magnetosphere. The model uses an analytical solution of the field-aligned force equation, including the ambipolar electric field, to determine the equatorial ion densities and scale heights as a function of  $L$ . Density contour plots for water group ions, hydrogen ions, and electrons are presented.

**Citation:** Persoon, A. M., et al. (2009), A diffusive equilibrium model for the plasma density in Saturn's magnetosphere, *J. Geophys. Res.*, 114, A04211, doi:10.1029/2008JA013912.

### 1. Introduction

[2] Between 1979 and 1981, the Pioneer 11, Voyager 1, and Voyager 2 spacecraft passed through Saturn's inner magnetosphere and acquired the first in situ plasma measurements in the vicinity of Saturn [Frank *et al.*, 1980; Trainor *et al.*, 1980; Wolfe *et al.*, 1980; Bridge *et al.*, 1981, 1982; Sittler *et al.*, 1983]. These measurements, along with remote sensing observations by the Hubble Space Telescope, were later used by Richardson and Sittler [1990], Richardson [1995, 1998], and Richardson and Jurac [2004] to develop plasma density models that were used to map the distribution of the electrons and ions in the planet's magnetosphere. On 1 July 2004, the Cassini spacecraft was placed in orbit around Saturn and began a multiyear mission to study the Saturnian system [Matson *et al.*, 2002], including state of the art instruments to study the plasma composition, density, and temperature in Sat-

urn's magnetosphere. One of the instruments contributing to these measurements is the Radio and Plasma Wave Science (RPWS) instrument. This instrument provides measurements of the electric and magnetic field spectrums of plasma waves over a frequency range from 1 Hz to 16 MHz with a time resolution on the order of a few seconds [Gurnett *et al.*, 2004]. Very precise electron densities can be derived from the RPWS electric field spectrums by measuring the frequency of upper hybrid resonance emissions [Moncuquet *et al.*, 2005; Persoon *et al.*, 2006b], which are detected over most of the inner region of Saturn's magnetosphere inside  $L = 10$ , where  $L$  is the McIlwain  $L$ -shell parameter [McIlwain, 1961]. The RPWS also includes a Langmuir probe that can provide electron temperature and density measurements [Wahlund *et al.*, 2005].

[3] The first attempt to model the RPWS electron densities focused on the early equatorial electron density measurements, which were shown to vary as  $n_e \propto R^{-3.7}$  where  $R$  is the radial distance in the equatorial plane [Persoon *et al.*, 2005]. By 30 October 2005, sufficient high-latitude electron densities were available to compare the measured electron densities to a latitudinal scale height model for a single ion species plasma based on a simple centrifugal force model. Using these data, Persoon *et al.* [2006a] were able to show that the equatorial plasma density varies as  $L^{-4.1}$  and that the corresponding plasma scale height varies as  $L^{1.8}$ . However, the orbital coverage available at that time only provided density measurements for latitudes below 20°, where the water group ion component is the largest component of the plasma. The model was unable to resolve a second lighter ion component, which would dominate the plasma at higher latitudes.

<sup>1</sup>Department of Physics and Astronomy, University of Iowa, Iowa City, Iowa, USA.

<sup>2</sup>Institute of Atmospheric Physics, Prague, Czech Republic.

<sup>3</sup>Faculty of Mathematics and Physics, Charles University, Prague, Czech Republic.

<sup>4</sup>Mullard Space Science Laboratory, University College London, Dorking, UK.

<sup>5</sup>Space and Atmospheric Science Group, Los Alamos National Laboratory, Los Alamos, New Mexico, USA.

<sup>6</sup>Swedish Institute of Space Physics, Uppsala, Sweden.

<sup>7</sup>Laboratoire d'Etudes Spatiales et Instrumentation en Astrophysique, Observatoire de Paris, Meudon, France.

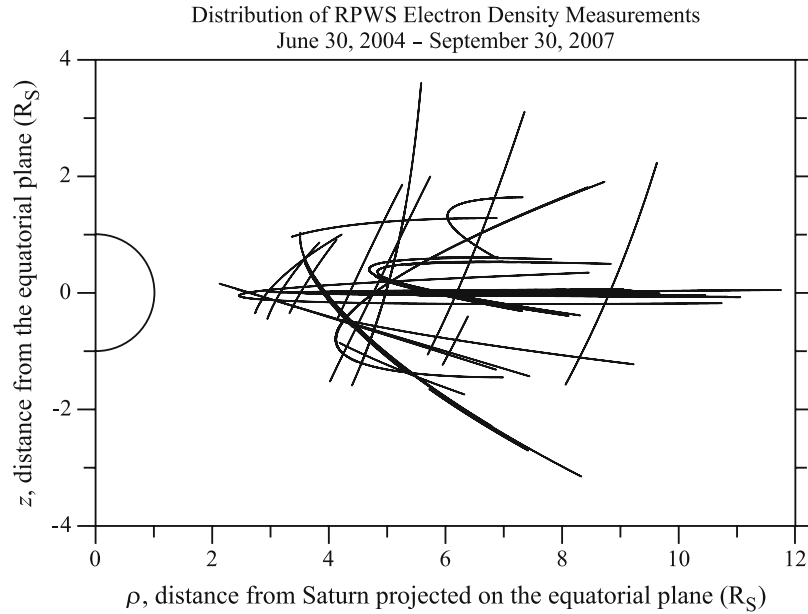


**Figure 1.** A plot in Saturn's meridian plane showing the distribution of Radio and Plasma Wave Science (RPWS) electron density measurements obtained between 30 June 2004 and 30 September 2007. The  $z$  coordinate is the distance above/below Saturn's equatorial plane, and  $\rho$  is the perpendicular distance from Saturn's spin axis. The greater latitudinal spread in the density measurements makes it possible to isolate both of the major ion components of the plasma in the inner magnetosphere.

[4] By 30 September 2007, Cassini had completed more than 50 orbits through Saturn's inner magnetosphere and the RPWS had acquired nearly 200,000 electron density measurements, extending up to latitudes of  $35^\circ$ , which is sufficiently high to resolve the hydrogen ion component. A meridian plane plot showing the spatial distribution of the electron density measurements for these orbits is presented in Figure 1. Our objective in this paper is to use these data to develop a diffusive equilibrium model for the thermal plasma in Saturn's inner magnetosphere based on an analytic solution of the diffusive equilibrium equations. These equations incorporate all of the relevant magnetic field-aligned forces acting on the plasma and allow us to determine the spatial distribution of the two major ion components in terms of equatorial ion densities and scale heights.

## 2. Diffusive Equilibrium Model

[5] Four primary forces act on a charged particle constrained to move along a magnetic field line in a rapidly corotating magnetosphere such as Saturn's. These are (1) the centrifugal force, (2) the magnetic mirror force, (3) the gravitational force, and (4) the ambipolar electric field force. For an equatorial particle corotating in Saturn's magnetic field, the centrifugal force is significantly greater than the gravitational force at radial distances beyond  $\sim 1.6$  Saturn radii ( $R_S$ ). A consequence of the dominance of the centrifugal force is that, beyond  $1.6 R_S$ , the plasma tends to accumulate in a disk-shaped region near the equatorial plane, called the plasma torus [Bridge *et al.*, 1982; Scarf *et al.*, 1984] or plasmasphere [Sittler *et al.*, 1983; Young *et al.*, 2005]. The magnetic mirror force, which acts to reflect the particles from the region of stronger magnetic field near

the planet, also acts to concentrate the plasma near the equator. These tendencies to concentrate the particles near the equatorial plane are opposed by the thermal motions in the plasma which tend to diffuse the particles outward, away from the equator. The resulting balance between these two competing effects determines the north-south thickness of the plasma disk and is usually described in terms of a scale height [Gledhill, 1967; Hill and Michel, 1976]. The ambipolar electric field force arises because the thermal velocity of the electrons is much higher than the thermal velocity of the ions, owing to the smaller mass of the electrons. In the absence of any other constraint, the electrons would rapidly escape along the magnetic field lines away from the equator. Instead, the escaping electrons quickly produce a polarization charge which causes a magnetic field-aligned electric field, called the ambipolar electric field, that confines the electrons to the plasma disk. This electric field has the opposite effect on the ions, drawing the ions away from the equator and increasing the scale height of the ions compared to what would occur if there were no ambipolar field.

[6] These physical processes can be quantitatively described by the magnetic field-aligned force equation for the  $i$ th species given by Richardson and Sittler [1990]:

$$\begin{aligned} \frac{\partial P_{\parallel i}}{\partial s} = & (P_{\parallel i} - P_{\perp i}) \frac{1}{B} \frac{\partial B}{\partial s} + n_i m_i \frac{\partial}{\partial s} \left( \frac{1}{2} \Omega^2 \rho^2 \right) \\ & + n_i \frac{\partial}{\partial s} \left( \frac{GM_S m_i}{r} \right) - n_i q_i \frac{\partial \Phi}{\partial s}. \end{aligned} \quad (1)$$

The term on the left-hand side of equation (1) is the parallel pressure gradient force, where  $P_{\parallel}$  is the parallel pressure and  $s$  is the distance along the magnetic field line. The first term on the right-hand side of equation (1) is the magnetic mirror

force, where  $B$  is the magnetic field strength and  $P_{\perp}$  is the perpendicular pressure. The second term on the right-hand side is the centrifugal force, where  $n_i$  and  $m_i$  are the number density and mass of the  $i$ th species,  $\Omega$  is the rotation rate of the plasma, and  $\rho$  is the distance measured from Saturn's spin axis. The third term on the right-hand side is the gravitational force, where  $G$  is the gravitational constant,  $M_S$  is the mass of Saturn and  $r$  is the planetocentric radial distance. The last term is the ambipolar electric field force, where  $q_i$  is the charge and  $\Phi$  is the electrostatic potential.

[7] To develop a useful analytical model to compare with our electron density measurements, we have integrated equation (1) along the magnetic field line in order to obtain an equation for the number density  $n_i$  of the  $i$ th species as a function of latitude  $\lambda$ , equatorial density  $n_{ieq}$ , plasma scale height  $H_i$ ,  $L$  value, the ion anisotropy  $A_i$  and the ambipolar electrostatic potential  $\Phi$ . Since Saturn's magnetic axis is aligned within one degree of its rotational axis [Connerney *et al.*, 1984], we have assumed that the magnetic field is a perfect dipole with the dipole axis aligned along the rotational axis. We have also assumed that the plasma rotates at the nominal rotation period of the planet, 10 h 39.4 min [Kaiser *et al.*, 1984], and that the electron temperature and ion anisotropies are constant along the magnetic field line. The assumption that the electron temperature and ion anisotropies are independent of latitude is almost certainly valid near the equator where most of our data are obtained, but may be questionable at higher latitudes.

[8] The above assumptions allow the number density of the  $i$ th species to be expressed in closed form by the following equation:

$$n_i = n_{eqi} \exp \left[ -A_i \ell n \left[ \frac{1}{\cos^6 \lambda} (1 + 3 \sin^2 \lambda) \right]^{1/2} - \frac{1}{3} \frac{L^2}{H_i^2} (1 - \cos^6 \lambda) + \frac{\alpha \tan^2 \lambda}{L H_i^2} - \frac{\beta_i}{H_i^2} \Phi \right], \quad (2)$$

where  $n_{eqi}$  is the equatorial number density,  $A_i = (T_{\perp i} / T_{\parallel i}) - 1$  is the ion anisotropy,  $\alpha$  and  $\beta_i$  are constants that are defined in Appendix A, and  $H_i$  is the dimensionless scale height

$$H_i = \sqrt{\frac{2\kappa T_{\parallel i}}{3m_i \Omega^2 R_S^2}}, \quad (3)$$

where  $R_S$  is the radius of Saturn. The scale height in units of kilometers can be calculated from  $H_i$  by multiplying by the radius of Saturn,  $R_S = 60,268$  km. A complete derivation of equation (2) is given in Appendix A.

[9] To see how the above equations are used in our analysis, it is useful to explicitly write out the corresponding equation for each species in the plasma, the water group ions ( $W^+$ ), the hydrogen ions ( $H^+$ ) and the electrons (e). The density of the water group ions is given by

$$n_{W^+} = n_{eqW^+} \exp \left[ -A_{W^+} \ell n \left[ \frac{1}{\cos^6 \lambda} (1 + 3 \sin^2 \lambda) \right]^{1/2} - \frac{1}{3} \frac{L^2}{H_{W^+}^2} (1 - \cos^6 \lambda) + \frac{\alpha \tan^2 \lambda}{L H_{W^+}^2} - \frac{\beta_{W^+}}{H_{W^+}^2} \Phi \right], \quad (4)$$

and the density of the hydrogen ions is given by

$$n_{H^+} = n_{eqH^+} \exp \left[ -A_{H^+} \ell n \left[ \frac{1}{\cos^6 \lambda} (1 + 3 \sin^2 \lambda) \right]^{1/2} - \frac{1}{3} \frac{L^2}{H_{H^+}^2} (1 - \cos^6 \lambda) + \frac{\alpha \tan^2 \lambda}{L H_{H^+}^2} - \frac{\beta_{H^+}}{H_{H^+}^2} \Phi \right]. \quad (5)$$

For the electrons, the corresponding equation can be greatly simplified. Because the electron mass is very small compared to the ion masses, it is easy to show that the centrifugal and gravitational terms are negligible. Also, since the thermal electrons experience considerable pitch angle scattering [Rymer *et al.*, 2007], we can assume to a good approximation that the electrons are isotropic, that is,  $A_e = (T_{\perp e} / T_{\parallel e}) - 1 = 0$ , which eliminates the mirror term. The only surviving term is the ambipolar term which, with the help of equation (3) and the definition of  $\beta$  found in Appendix A, can be written as

$$n_e = n_{eqe} \exp \left[ \frac{\Phi}{W_e} \right], \quad (6)$$

where  $W_e = \kappa T_{\parallel e} / e$  is the electron temperature expressed in electron volts. Since the electron density must satisfy the charge neutrality condition at all points along the magnetic field line,

$$n_e = n_{W^+} + n_{H^+}, \quad (7)$$

the equatorial electron density is given by

$$n_{eqe} = n_{eqW^+} + n_{eqH^+}. \quad (8)$$

Substituting equation (8) into equation (6) gives the electron density in terms of the ion equatorial densities:

$$n_e = [n_{eqW^+} + n_{eqH^+}] \exp \left[ \frac{\Phi}{W_e} \right]. \quad (9)$$

The ion equatorial densities and ion scale heights are determined by fitting the charge neutrality condition, equation (7), to the measured electron densities using equations (4), (5), and (9). The electrostatic potential must be numerically solved at each point along the integration path using equations (7) and (9).

### 3. Electron Temperature and Ion Anisotropies

[10] Inspection of equations (4), (5), and (9) shows that the electron density is controlled by seven parameters, two equatorial ion densities  $n_{eqW^+}$  and  $n_{eqH^+}$ , two scale heights  $H_{W^+}$  and  $H_{H^+}$ , the electron temperature  $W_e$ , and two ion anisotropies  $A_{W^+}$  and  $A_{H^+}$ , all of which depend on  $L$ . Although the  $L$  dependence of these parameters could in principle be determined by performing a least squares best fit to the observed latitudinal electron density distribution along a given  $L$  shell, in practice the electron temperature and the two ion anisotropies are poorly constrained by such a fitting procedure. Fortunately, these parameters are easily determined by direct in situ measurements.

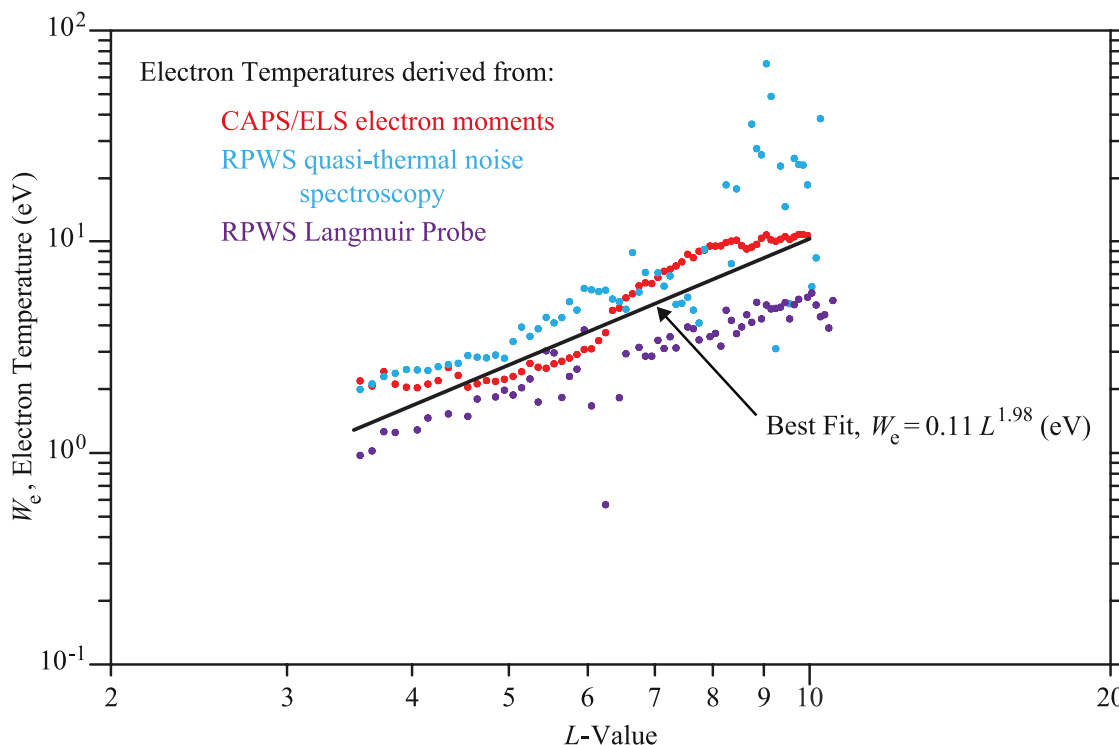


**Figure 2.** The  $L$ -value distribution of electron temperatures obtained from Cassini Plasma Electron Spectrometer (CAPS/ELS) (red dots), averaged over one  $L$  value and smoothed with a sliding average in increments of 0.1. Since the CAPS/ELS measurements have not been corrected for spacecraft potential, the temperatures tend to be warmer, especially at low temperatures close to Saturn. Also shown in Figure 2 are the electron temperatures derived from the spectroscopy of high-frequency quasi-thermal noise emissions measured by RPWS during the Cassini orbit insertion, shown in blue dots [Moncuquet *et al.*, 2005], and the magnetospheric electron temperatures derived from the RPWS Langmuir probe measurements during Cassini orbit insertion, shown as violet dots [Wahlund *et al.*, 2005]. The RPWS measurements are not affected by the spacecraft potential. The fit to the average of the three data sets (black line) shows a power law fit with temperature varying as  $L^{1.98}$ .

[11] The electron temperature can be measured by three methods: (1) from the Cassini Plasma Electron Spectrometer (CAPS/ELS) using an integral moment method described by Lewis *et al.* [2008], (2) from the RPWS using quasi-thermal noise spectroscopy as described by Moncuquet *et al.* [2005], and (3) from the RPWS using the Langmuir probe as described by Wahlund *et al.* [2005]. Figure 2 shows a plot of the electron temperature obtained using these three techniques for a range of  $L$  values,  $3.6 \leq L \leq 10$ . Since we are interested in the thermal component of the electron energy distribution, in all three cases we have focused on the cold electron temperatures. In the case of the CAPS/ELS data (Figure 2, red dots), temperatures were calculated from logarithmically spaced energy bins near the lower energy range of the instrument, from 0.58 to 100 eV. In the case of the RPWS quasi-thermal spectroscopy data (Figure 2, blue dots), we have used the “core” electron temperatures, as published by Moncuquet *et al.* [2005]. In the case of the RPWS Langmuir probe data (Figure 2, violet dots), we have used the temperature of the cold magnetospheric electron component, as published by Wahlund *et al.* [2005]. The three techniques are in generally good agreement, within approximately a factor of 2. All three techniques show that the electron temperature increases

systematically with increasing  $L$  value, varying as a straight line on the log-log plot. The straight line fit indicates a power law dependence, with the electron temperature varying as  $W_e = 0.11L^{1.98}$  eV. This best fit  $L$  dependence for the electron temperature will be used throughout our subsequent analysis. Note that the exponent in the power law is very close to two, which means that the “core” electron temperature is proportional to the corotational energy, consistent with the observations of Rymer *et al.* [2007].

[12] For the ion anisotropies we rely on measurements from the Cassini Plasma Spectrometer (CAPS), which are difficult to obtain because, typically, the CAPS instrument is not able to sample the entire distribution function owing to pointing constraints imposed by the nonspinning spacecraft. Figure 3 shows the anisotropies obtained from best fits to the CAPS ion data from a series of equatorial orbits in 2005 and 2006, assuming bi-Maxwellian phase space density functions characterized by  $T_{\perp}$  and  $T_{\parallel}$  for both the water group ions (Figure 3, top) and the hydrogen ions (Figure 3, bottom). For radial distances greater than  $L = 5.5$ , the plasma data from these dayside equatorial orbits are analyzed using a forward modeling technique [Wilson *et al.*, 2008]. Inside  $L = 5.5$  and within the high-density neutral Enceladus torus, both the water group ion distribution [Tokar *et al.*, 2008]

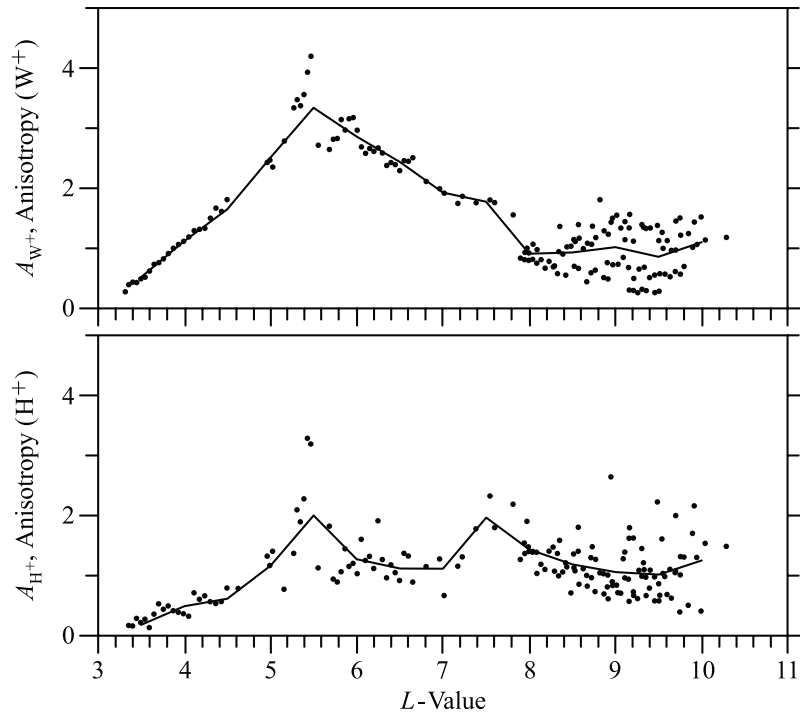


**Figure 3.** The  $L$ -value distribution of the ion anisotropies, obtained from fits to the CAPS ion data, assuming anisotropic Maxwellian phase space density functions for both the water group ions (top) and the hydrogen ions (bottom), shown as black dots. A smoothly varying distribution of ion anisotropies is obtained by averaging the data in nonoverlapping  $L$ -shell bins of 0.5 and using a piecewise linear fit between these data points, shown as solid black lines.

and the hydrogen ion distribution have highly anisotropic pick-up ion components, which will contribute to the mirror force acting on the ions. In this study, both the ion core and pickup distributions inside  $L = 5.5$  are fit to a single bi-Maxwellian to obtain the temperature anisotropies shown in Figure 3. The ion anisotropies are then averaged in nonoverlapping  $L$ -shell bins of 0.5. A smoothly varying distribution of ion anisotropies for the diffusive equilibrium model is obtained using a piecewise linear fit between the averaged points, shown as a solid black line in both plots of Figure 3.

#### 4. Relative Importance of the Various Terms in the Density Equation

[13] Since the equations needed to compute the electron density are quite complicated, before proceeding further it is useful to first investigate the relative importance of the various terms in equation (2). The procedure that we have adopted to investigate these terms is to generate a simulated electron density data set based on a centrifugal potential model with no mirror force, no gravitational force, and no ambipolar electric field force, and then introduce the additional terms one at a time in order to evaluate their effect on the basic fit parameters,  $n_{eqW^+}$ ,  $n_{eqH^+}$ ,  $H_{W^+}$ , and  $H_{H^+}$ . We start with a purely centrifugal potential model because this model has been shown to provide a good fit to the RPWS electron densities at low latitudes where the water group ions are the dominant plasma component [Persoon *et al.*, 2006a]. One of our key objectives will be to determine if

the centrifugal potential model also provides a good fit at higher latitudes where the hydrogen ions are the dominant component.

[14] To limit the number of variables, we start by focusing on  $L = 6.4$  which is roughly in the middle of the  $L$ -value range for which we have data. Later, we investigate the effect of varying the  $L$  value on each of the terms in the model. The effect of adding the gravitational term, the water group ion mirror term, the hydrogen ion mirror term, and the ambipolar term to the centrifugal term are illustrated in Figures 4–7, respectively. These plots show the natural log of the ion and electron densities computed from equations (4) and (5) and the charge neutrality from equation (7) as functions of  $(1 - \cos^6 \lambda)$ , which is the linear variable associated with the centrifugal force term [Persoon *et al.*, 2006a]. The straight solid black lines labeled  $n_{W^+}$  and  $n_{H^+}$  are the water group and hydrogen ion densities. The upper, curved black line is the electron density,  $n_e = n_{W^+} + n_{H^+}$ . The black dots in Figures 4–7 are the simulated electron density data, generated using only the centrifugal potential term,  $-(1/3)(L^2/H^2)(1 - \cos^6 \lambda)$ , with all of the other terms set to zero. In the absence of the other terms, the ion densities are straight lines in Figures 4–7. The parameters used for generating the simulated data are  $n_{eqW^+} = 20.92 \text{ cm}^{-3}$ ,  $n_{eqH^+} = 4.49 \text{ cm}^{-3}$ ,  $H_{W^+} = 0.92$ , and  $H_{H^+} = 4.11$ . Using equation (8), these equatorial ion densities are found to be consistent with the equatorial electron density results of Persoon *et al.* [2006a]. The ion scale heights are consistent with the results presented later in this paper.

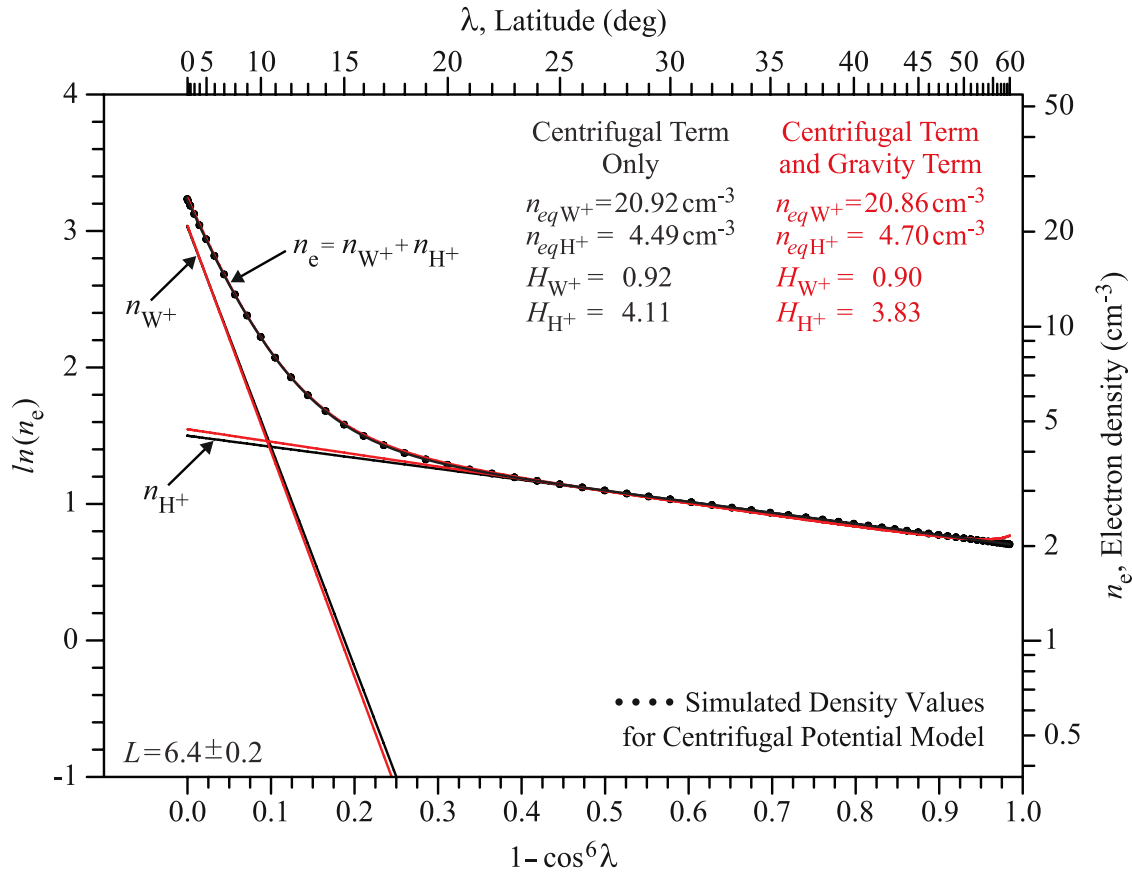


**Figure 4.** A plot showing the simulated density values (black dots) for  $L = 6.4$  which provide a perfect fit for the centrifugal term only, as a function of the natural logarithm of the electron density and  $(1 - \cos^6 \lambda)$ . The electron density and latitude values are labeled on the right vertical axis and the top axis, respectively. The fit through the simulated density values is the solid black line. The solutions to equations (4) and (5) give the densities of the water group and hydrogen ions, labeled  $n_{W^+}$  and  $n_{H^+}$  (in black). The solid red lines show the density fit for the combined centrifugal and gravitational terms and the solutions to the density equations for the water group and hydrogen ions. As expected, the gravitational term has little effect on the relatively small mass of the ions for latitudes less than  $50^\circ$  with only small changes in the equatorial densities and plasma scale heights derived from the fit. The gravitational term becomes only slightly important at high latitudes near the foot of the magnetic field line.

[15] The effect of the gravity term,  $(\alpha/L) (\tan^2 \lambda / H_i^2)$ , on the best fit to the simulated data points is shown by the red lines in Figure 4. The fit is obtained by adjusting the parameters,  $n_{eqW^+}$ ,  $n_{eqH^+}$ ,  $H_{W^+}$ , and  $H_{H^+}$ , to obtain the best least squares fit to the simulated data points using equations (4) and (5) and the charge neutrality condition, neglecting the ambipolar and mirror terms. The best fit parameters (in red) are listed in Figure 4. The gravity term has little effect on the fit parameters. In fact the change is so small that the best fit electron density profile (Figure 4, curved red line) cannot be distinguished from the black line through the simulated data points, except at very high latitudes. This is the expected result, since the centrifugal force is substantially greater than the gravitational force at radial distances beyond  $\sim 1.6 R_S$ . Gravity does become important near the foot of the magnetic field line at latitudes of above  $50^\circ$  for  $L = 6.4$ . However, our data never extends to such high latitudes.

[16] The effect of the mirror force term,  $A_i \ell n [(1 + 3 \sin^2 \lambda)^{1/2} / \cos^6 \lambda]$ , on the best fit to the simulated data points is shown by the colored lines in Figures 5 and 6 for several water group and hydrogen ion anisotropies. The best fit to the simulated data points is obtained by using equations (4), (5), and (7), neglecting the gravitational and ambipolar terms. The selected anisotropies are consistent with the measured anisotropies given in Figure 3. In Figure 5 the mirror term has essentially no effect on the fit parameters for the water group ions, even for relatively large anisotropies,  $A_{W^+} = 5$ . The reason the water group ion anisotropy has a negligible effect is that these ions have a relatively small scale height, which concentrates them very close to the equator where the mirror term  $\ell n (B/B_0)$  is very small (equation (A10) in Appendix A). In sharp contrast, Figure 6 shows that the mirror term for the hydrogen ions has a considerable effect, even for relatively small anisotropies,  $A_{H^+} = 1$ . The reason that the mirror term is more important for the hydrogen ions is that these particles extend

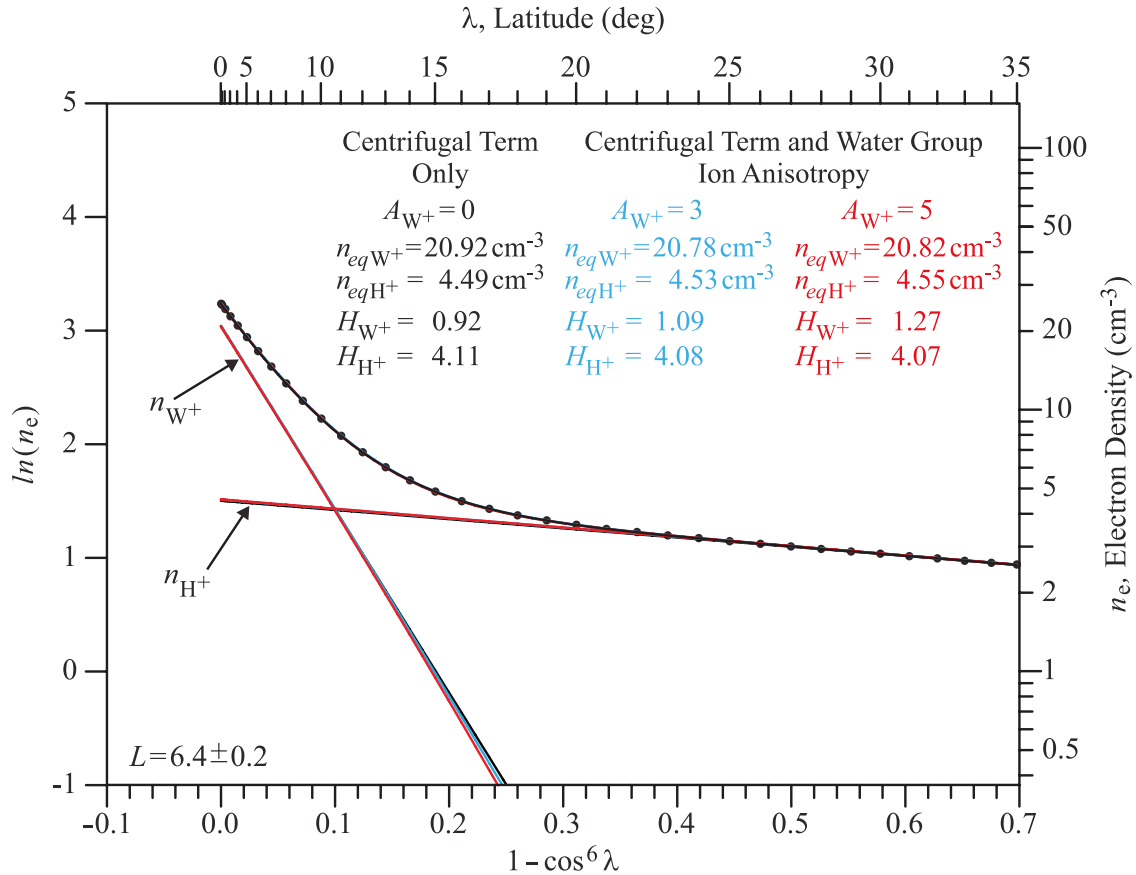


**Figure 5.** A plot showing the density fit to the same simulated density values (black dots) shown in Figure 4 at  $L = 6.4$  for the centrifugal term alone (black lines) and for the combined centrifugal and mirror terms for two water group ion anisotropies (colored lines). In this plot, the hydrogen ion anisotropy has been set to zero. The equatorial ion densities and ion scale heights are listed in colors corresponding to the water group ion anisotropies used in the fit. The addition of the mirror term to the model has little effect on the water group ion densities over a wide range of water group ion anisotropies, indicating that the mirror term is not significant for this ion species.

much farther from the equator, where the  $\ln(B/B_0)$  term is no longer negligible. As a result the best fit parameters for the hydrogen ions are quite sensitive to the hydrogen ion anisotropies given in Figure 3. We will return to this point later.

[17] The effect of the ambipolar electric field term,  $-\beta_i \Phi / H_i^2$ , is shown in Figure 7 for a range of electron temperatures consistent with those in Figure 2. The electron temperature has a considerable effect on the latitudinal profiles, especially for the hydrogen ion densities near the equator. This dependence arises because the ambipolar electric field force increases with increasing temperature, which tends to draw the lighter hydrogen ions farther from the equator, thereby decreasing the hydrogen ion equatorial density. Increasing the temperature has little effect on the water group ions, which are much heavier and concentrated closer to the equator by the larger centrifugal force. Despite these effects, the electron temperature has an almost negligible effect on the overall fit of the electron density profile to the simulated electron density data. This means that the electron temperature cannot be reliably determined from the

electron density data alone, but must be obtained from independent measurements (Figure 2).

[18] To illustrate how the terms discussed above vary with radial distance, Figures 8 and 9 show the relative contributions of each term in equation (2) for selected  $L$  values from 3.6 to 9.6. Each term has been normalized by dividing by the centrifugal term. Figure 8 shows the relative contribution of each term on the distribution of the water group ions, and Figure 9 shows the relative contribution of each term on the distribution of the hydrogen ions. The scale heights used to compute these ratios are assumed to vary as  $H_{W^+} = 0.045L^{1.5}$  and  $H_{H^+} = 0.306L^{1.4}$  which are consistent with the best fit results that will be presented later in this paper. The relative contribution of the ambipolar term is evaluated for electron temperatures taken from the values in Figure 2, and the relative contribution of the mirror term for both ion species is evaluated for  $A_{W^+} = A_{H^+} = 1$ . Figure 8 shows that the centrifugal term is the dominant term for the water group ions over the entire range of  $L$  values from  $3.6 \leq L \leq 9.6$ . This is because of the concentration of water group ions near the magnetic equator where the gravity, mirror, and ambipolar terms are small. This means

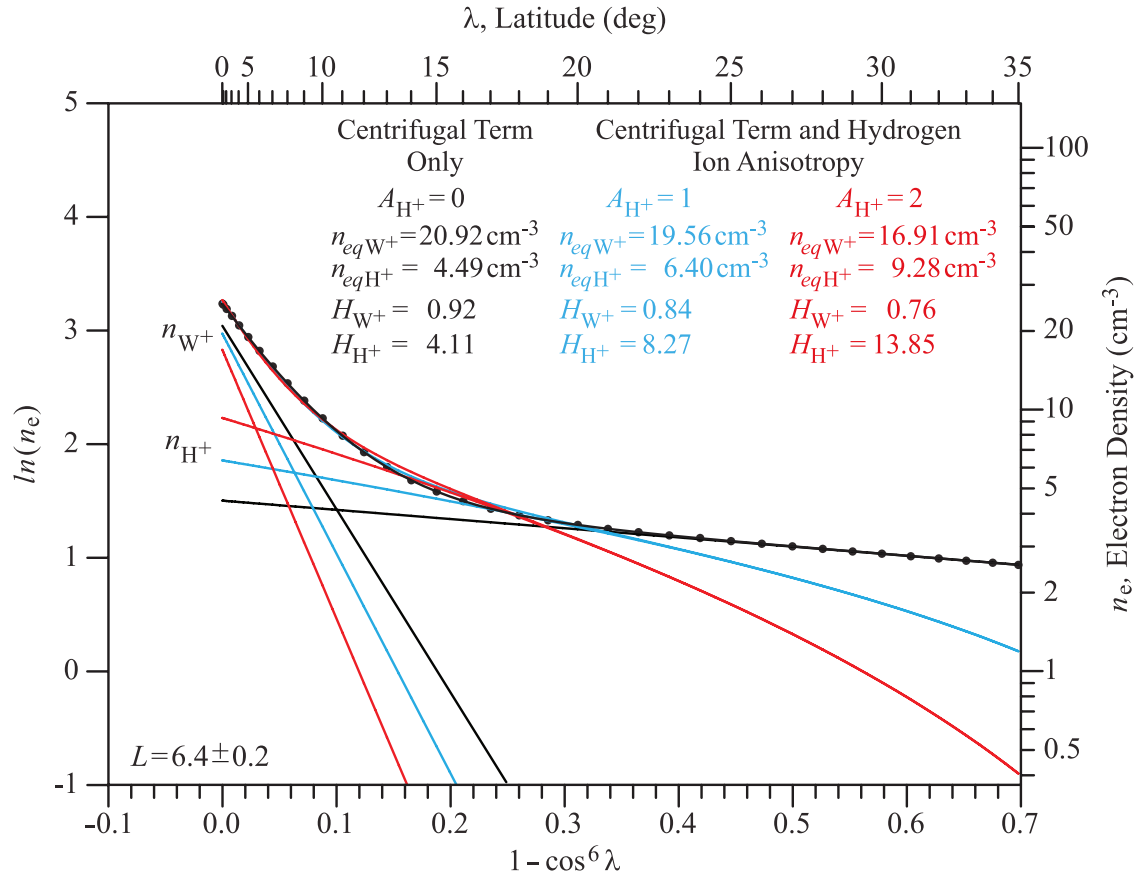


**Figure 6.** A plot showing the density fit to the same simulated density values (black dots) shown in Figure 4 at  $L = 6.4$  for the centrifugal term alone (black lines) and for the combined centrifugal and mirror terms for two hydrogen ion anisotropies (colored lines). In this plot, the water group ion anisotropy has been set to zero. The mirror term has a significant effect on the hydrogen ion distribution, even for the small anisotropy values. The inclusion of the hydrogen ion anisotropy raises the equatorial density and strongly suppresses the density at high latitudes. This parameter controls the density fit in the high-latitude region of the magnetosphere.

that the electron temperature and water group anisotropy measurements given in Figures 2 and 3 have relatively little influence on the best fit parameters for the water group ions.

[19] Figure 9 shows that the situation for the hydrogen ions is quite different. Close to the planet, the ambipolar term is the dominant term in determining the distribution of hydrogen ions. For most of the  $L$  values and especially at low latitudes, the relative contributions from the mirror and ambipolar terms are larger than from the centrifugal term. The ambipolar term is particularly important at low latitudes and small  $L$  values where, because of the minus sign in equation (2), it strongly suppresses the hydrogen ion density. The mirror term is of minor importance at low  $L$  values but becomes increasingly important as the  $L$  value increases, becoming comparable to the ambipolar term at low latitudes. This  $L$  dependence is due to the rapid increase in the hydrogen ion scale height with increasing  $L$ , which tends to decrease the importance of the centrifugal term relative to the mirror term (equation (2)). Since both the ambipolar and mirror terms are important, the best fit parameters for the hydrogen ion component are quite sensitive to variations in

the electron temperature and hydrogen ion anisotropy measurements given in Figures 2 and 3.

## 5. Fitting the Diffusive Equilibrium Model to the Measured Electron Densities

[20] To fit the measured electron densities with the diffusive equilibrium model, the RPWS electron densities are grouped into  $L$ -shell bins of 0.4 and then averaged in one-degree latitude bins. Equations (4), (5), and (9) are used to satisfy the charge neutrality of equation (7), using electron temperatures and ion anisotropy values from Figures 2 and 3. Figure 10 shows the measured RPWS electron densities, plotted as  $\ln(n_e)$  versus  $(1 - \cos^6 \lambda)$  for the  $L = 6.4$  bin, the same  $L$ -shell bin evaluated in Figures 4–7 for the simulated densities. The corresponding electron density scale is shown along the right vertical axis, and the corresponding latitude scale is shown along the top axis. The measured densities (Figure 10, black dots) range from  $26.8 \text{ cm}^{-3}$  at  $\lambda = 2.3^\circ$  to  $3.1 \text{ cm}^{-3}$  at  $\lambda = 19.4^\circ$ . The solution to the charge neutrality condition  $n_e = n_{W^+} + n_{H^+}$  is the curved red line and represents the fit of the model to



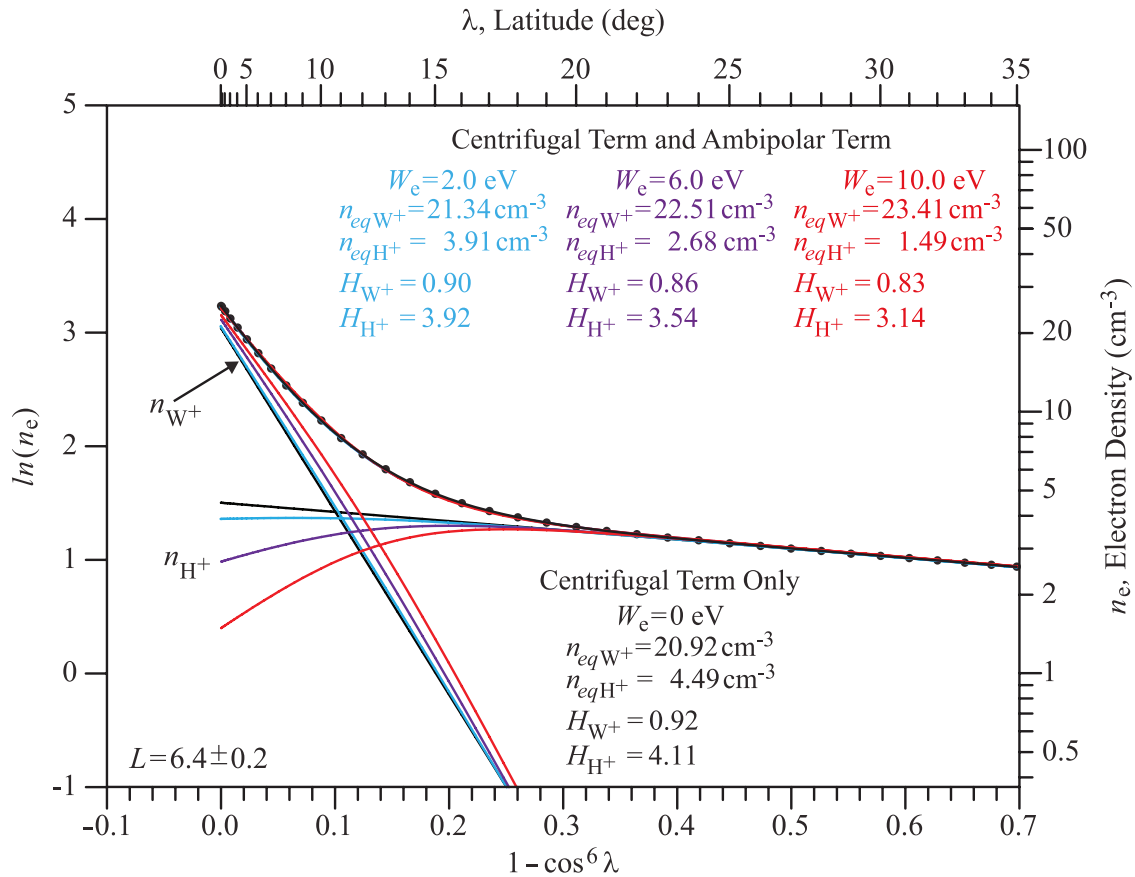


**Figure 7.** A plot showing the density fit to the same simulated density values as those in Figure 4 for the centrifugal term alone (black lines) and for the combined centrifugal and ambipolar terms for three electron temperatures, ranging from 2 to 10 eV (colored lines). The equatorial ion densities and ion scale heights are listed in colors corresponding to the electron temperatures used in the fit. The ambipolar term has only a slight effect on the distribution of the water group ions as the electron temperature increases. But the effect on the hydrogen ions is very strong for all latitudes below  $20^\circ$ , with the equatorial densities and scale heights decreasing as the ambipolar electric field force increases with increasing electron temperature. However, the increasing electron temperature has little effect on the overall fit to the simulated electron density values, indicating that the diffusive equilibrium model is not sensitive to this input parameter.

the measured densities. The solutions to the water group and hydrogen ion densities, given by equations (4) and (5), are labeled near their intercepts at  $\lambda = 0$ . The diffusive equilibrium model is a least squares fit in four-parameter ( $n_{eqW^+}$ ,  $n_{eqH^+}$ ,  $H_{W^+}$ , and  $H_{H^+}$ ) space. Figures 10a and 10b show the local minima in chi-square [Bevington and Robinson, 1992] as functions of the equatorial density and scale height for the water group ions and the hydrogen ions, respectively. The best fit to the measured densities for the  $L = 6.4$  bin gives  $n_{eqW^+} = 21.64$  cm $^{-3}$ ,  $n_{eqH^+} = 3.77$  cm $^{-3}$ ,  $H_{W^+} = 0.97$ , and  $H_{H^+} = 1.97$ .

[21] Figure 11 is a multipanel plot in the same format as that of Figure 10, showing the diffusive equilibrium model fit to the RPWS electron densities in seven  $L$ -shell bins from 3.6 to 9.6. The diffusive equilibrium model provides an excellent fit to the measured RPWS densities throughout the inner magnetosphere. At low latitudes, the ambipolar term influences the hydrogen ion distribution, suppressing the equatorial densities and shifting the peak of the hydrogen

ion distribution to higher latitudes with increasing  $L$  value ( $\lambda \geq 10^\circ$ ) as the hydrogen ion torus expands. At higher  $L$  values, the mirror term effect can be seen in the downward trend to the density fit at high latitudes. In the lower three plots, the mirror term is the primary term that controls the fit to the electron densities at high latitudes.

[22] The diffusive equilibrium model fit to the measured densities for 0.2 increments in  $L$  shell yields best values for each of the four parameters in the fit, the equatorial densities and the plasma scale height for the two ion species. Using these results, we investigate how the equatorial densities and plasma scale heights vary with  $L$ . The equatorial densities obtained from the diffusive equilibrium fit to the RPWS electron densities for  $3.6 \leq L \leq 10.0$  are shown in Figure 12. Both equatorial density profiles peak inside  $L = 5$  just beyond the orbit of Enceladus, the result of the ionization of the water group neutrals emitted from the moon's southern geysers. The equatorial density profile for the water group ions peaks at  $62$  cm $^{-3}$  at  $L = 4.8$  and the

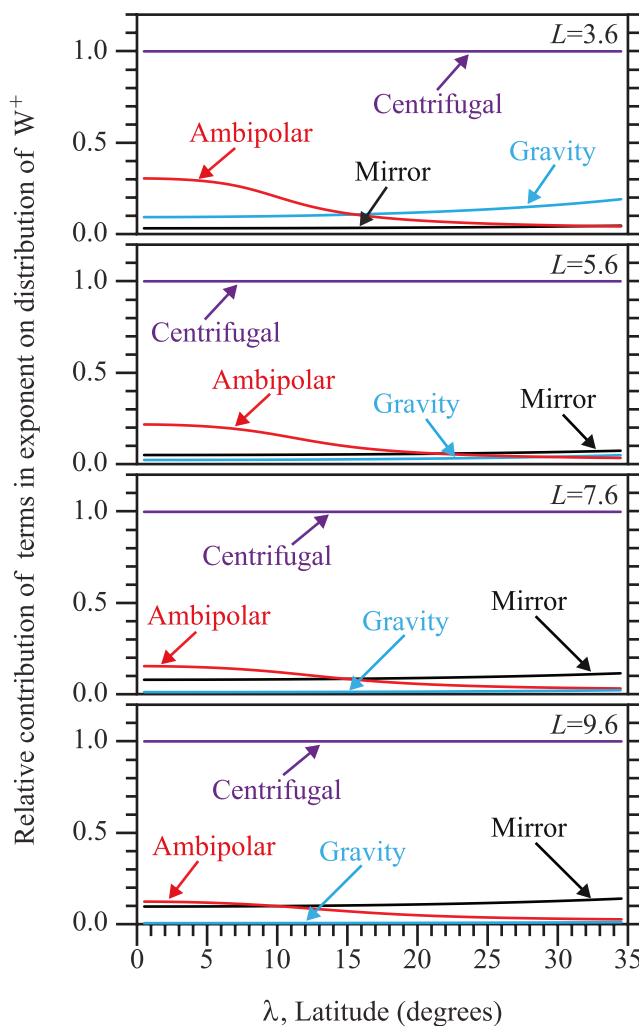


**Figure 8.** A multipanel plot for four  $L$  values, showing the contribution of each term in the exponent of the density equations to the distribution of the water group ions, assumed to be weakly anisotropic ( $A_{W^+} = 1$ ). All terms have been normalized to the centrifugal term, shown at the top of each plot. The centrifugal force is clearly the only significant force acting on the water group ions at all latitudes and  $L$  values.

equatorial density profile for the hydrogen ions peaks at  $9 \text{ cm}^{-3}$  at  $L = 4.6$ . Beyond  $L = 5$ , the best line fit through the water group ion densities decreases with increasing  $L$  value, varying as  $L^{-4.3}$ . The  $L$  dependence of the equatorial density profile for the dominant water group ions is in good agreement with the  $L$  dependence of  $L^{-4.1}$  found in the earlier centrifugal potential model of *Persoon et al.* [2006a] and with the  $L$  dependence of  $L^{-4.5}$  derived from CAPS ion plasma moments using a forward modeling technique [*Wilson et al.*, 2008]. The radial variation of the equatorial hydrogen ion densities is slower, varying as  $L^{-3.2}$ . Secondary peaks in the equatorial density profile for the hydrogen ions coincide with the peaks in the hydrogen ion anisotropy measurements (Figure 3). Larger hydrogen ion anisotropies increase the strength of the mirror force, elevating the equatorial densities at  $L \approx 5.5$  and  $L = 7.5$ .

[23] The plasma scale heights obtained from the diffusive equilibrium model fit to the RPWS electron densities for  $3.6 \leq L \leq 10.0$  are shown in Figure 13. For both ion species, the scale height expands with increasing  $L$  value, resulting in a thickening of the ion torus with increasing distance

from Saturn. Although the scale height for the water group ions is an order of magnitude smaller than the hydrogen ion scale height owing to the concentration of this species near the equatorial plane, both ion scale heights show a similar  $L$  dependence varying as  $L^{1.5}$  and  $L^{1.4}$  respectively. The ion temperatures corresponding to these ion scale heights have been derived using equation (3) and are shown on the right vertical axis of Figure 13. For both ion species, the temperatures range from several eV at  $L = 3.6$  to  $\sim 100$  eV at  $L = 10$ . These temperatures, derived from more than 3 years of density measurements, are approximately a factor of 3 lower than the mean ion temperatures derived from the CAPS measurements during Saturn orbit insertion [*Sittler et al.*, 2006; *Young et al.*, 2005]. The temperatures derived for the water group ions in Figure 13 are slightly lower than those found in the forward-modeled CAPS temperatures by a factor of 2 (see  $W^+T_{\parallel}$  (eV) in Table 2 of *Wilson et al.* [2008]) and show the same increase with increasing radial distance. However, there is no well-defined minimum in the water group ion temperatures at the Dione  $L$  shell in this study, possibly because the binning of the data and the

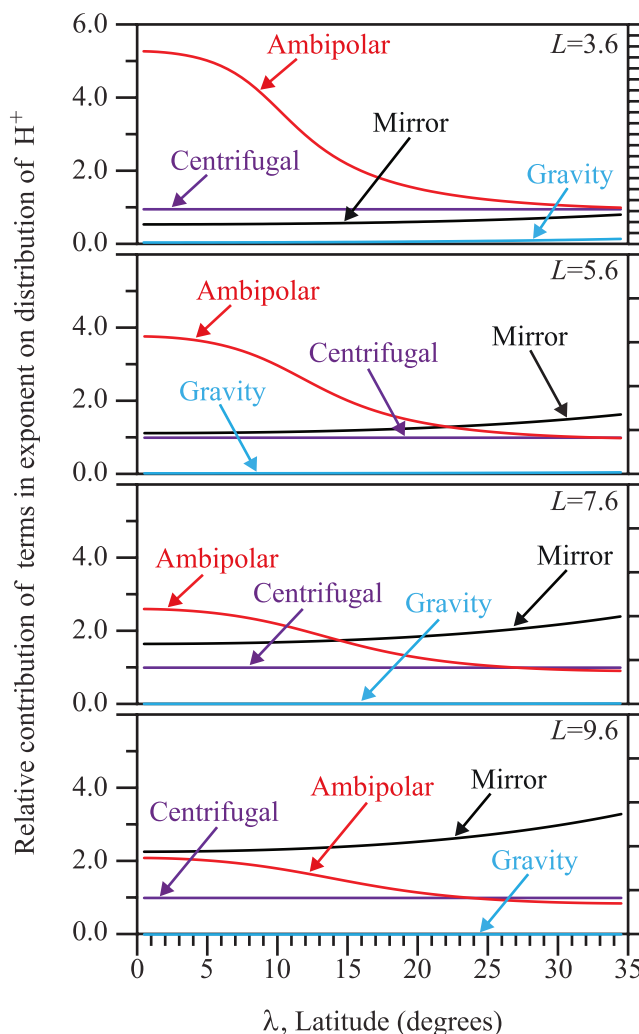


**Figure 9.** A multipanel plot for four  $L$  values, showing the contribution of each term in the exponent of the density equations to the distribution of the hydrogen ions, which are assumed to be weakly anisotropic ( $A_{H^+} = 1$ ). All terms have been normalized to the centrifugal term, shown near the bottom of each plot. The ambipolar and mirror terms dominate the distribution of the hydrogen ions in most regions of the magnetosphere. At lower  $L$  values below  $20^\circ$ , the ambipolar term is a significant factor in determining the distribution of the lighter ions, but the ambipolar term has diminishing importance at higher  $L$  values. The mirror term becomes increasingly important beyond  $L = 5$ , becoming comparable to the ambipolar term and opposing the ambipolar effect on the ion distribution.

sliding average technique used here would have masked a narrow minimum in the ion temperature. The hydrogen ion temperatures in Figure 13, which are similar to the water group ion temperatures, are greater than the hydrogen ion temperatures of *Wilson et al.* [2008] by nearly a factor of 4. However, there is a strong local minimum in the hydrogen ion temperature at the Dione  $L$  shell, similar to the minimum observed in the CAPS temperatures [*Wilson et al.*, 2008].

## 6. Density Contour Plots of the Three Plasma Components

[24] Density contour plots in the meridian plane ( $\rho, z$ ) have been constructed for each of the plasma species in order to visualize the distribution of plasma in Saturn's inner magnetosphere. The contour plots assume azimuthal symmetry about Saturn's rotational axis and mirror symme-

try about the equatorial plane. In order to produce smooth contours, the equatorial ion densities and ion scale heights in Figures 12 and 13 have been smoothed using a five-point sliding average to provide a functional  $L$ -value representation of these parameters for  $3.6 \leq L \leq 10$ . These smoothed values are iteratively used to construct a smoothed profile for the electrostatic potential as a function of  $L$  value. By inserting electron temperatures and ion anisotropies from Figures 2 and 3 and making the appropriate substitutions for the latitude and  $L$  value, equations (4) and (5) are used to compute the ion density at any point ( $\rho, z$ ) in the meridian plane.

[25] The contours of constant density for the water group ions are shown in the left plot of Figure 14. The density contours clearly show that the heavier ions are closely confined to the equatorial plane in the inner magnetosphere.

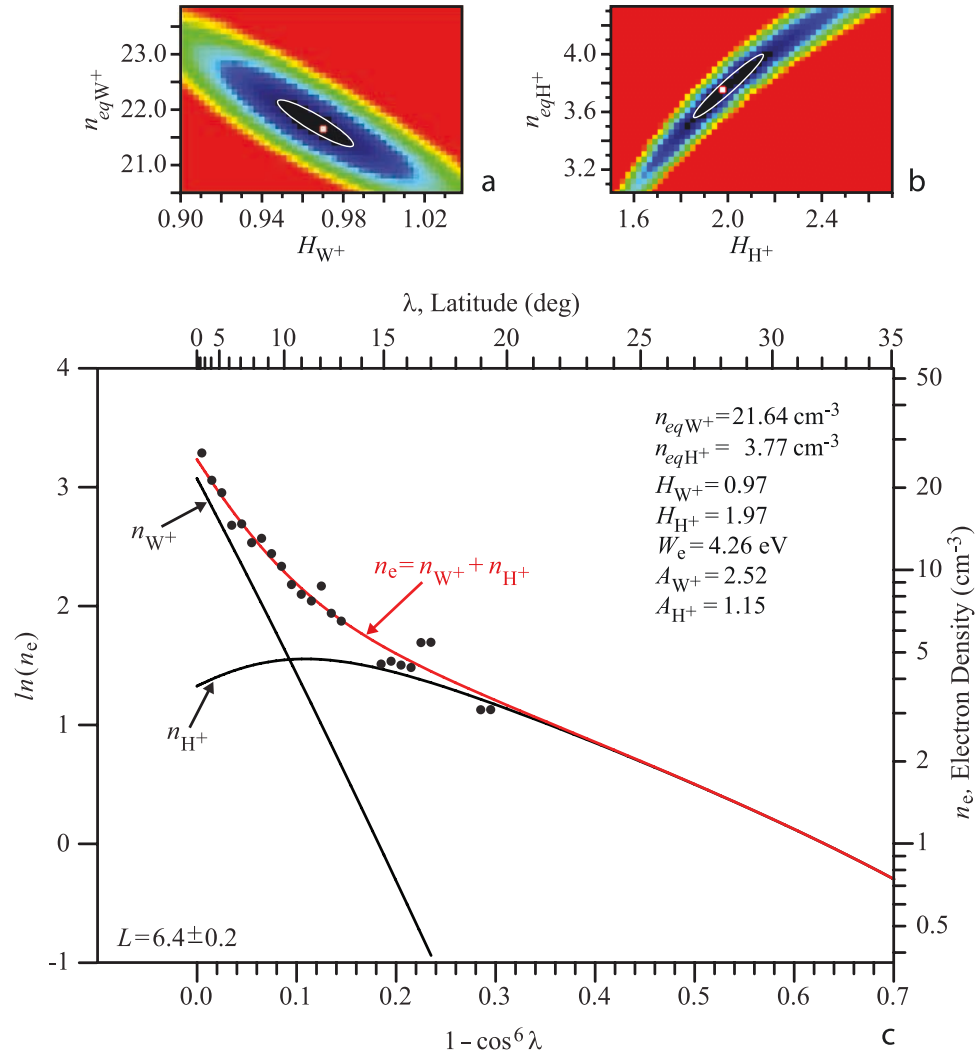


**Figure 10.** (a) The local minimum in chi-square for the water group ion parameters  $n_{eqW^+}$  and  $H_{W^+}$ . The region defined in black and bounded by a white oval indicates a good fit to the model. (b) The local minimum in chi-square for the hydrogen ion parameters  $n_{eqH^+}$  and  $H_{H^+}$ . (c) The measured RPWS electron densities for  $L = 6.4$ , plotted as the natural logarithm of the density and  $(1 - \cos^6 \lambda)$ . The corresponding density values are listed on the right vertical axis, and the latitude is given on the top axis. The solutions to the water group and hydrogen ion density equations (4) and (5) are labeled near their intercepts at  $\lambda = 0$ . The solution for the electron density,  $n_e = n_{W^+} + n_{H^+}$ , is given by the red line. The fit is a least squares fit in four-parameter space. The values for the ion equatorial densities and plasma scale heights obtained by the best fit method are listed in the upper right corner of Figure 10c.

Densities greater than  $30 \text{ cm}^{-3}$  are confined within  $|z| \leq 0.5 R_S$  of the equator and inside  $L = 6$ . Densities greater than  $5 \text{ cm}^{-3}$  are confined within  $|z| \leq 1 R_S$  of the equator inside  $L = 9$ . The contours of constant density for the hydrogen ions are shown in the right plot of Figure 14 and clearly show an ion population that is expanding rapidly away from the equatorial plane. The maximum density contour for  $n_{H^+} = 9 \text{ cm}^{-3}$  peaks off the equatorial plane out to  $z \approx 1 R_S$  for  $3.6 \leq L \leq 4$ , showing the influence of a strong ambipolar force lifting the lighter ions away from the equator in this region (see Figure 9).

[26] The electron density contours shown in Figure 15 are derived from the charge neutrality condition,  $n_e = n_{W^+} + n_{H^+}$ , using the ion densities derived for the ion density contour plots in Figure 14. The highest electron densities

( $n_e \geq 50 \text{ cm}^{-3}$ ) are found near the equatorial plane inside  $5.5 R_S$ . The contour map shows that the magnetospheric plasma is diffusing radially outward from the planet and away from the equatorial plane in Saturn's inner magnetosphere.

[27] The main features of the contour maps from Figures 14 and 15 are consistent with similar density contours derived by Richardson and Jurac [2004] and Sittler *et al.* [2008]. Richardson and Jurac [2004] developed their constant density contours by self-consistently solving for the neutral and ion densities, using a Monte Carlo model for the neutral density and a chemistry-transport model for the ion density, constrained by in situ density measurements obtained during the Saturn flybys of Voyagers 1 and 2 [Richardson, 1998]. Sittler *et al.* [2008] uses CAPS ion and electron fluid parameters as boundary conditions to solve

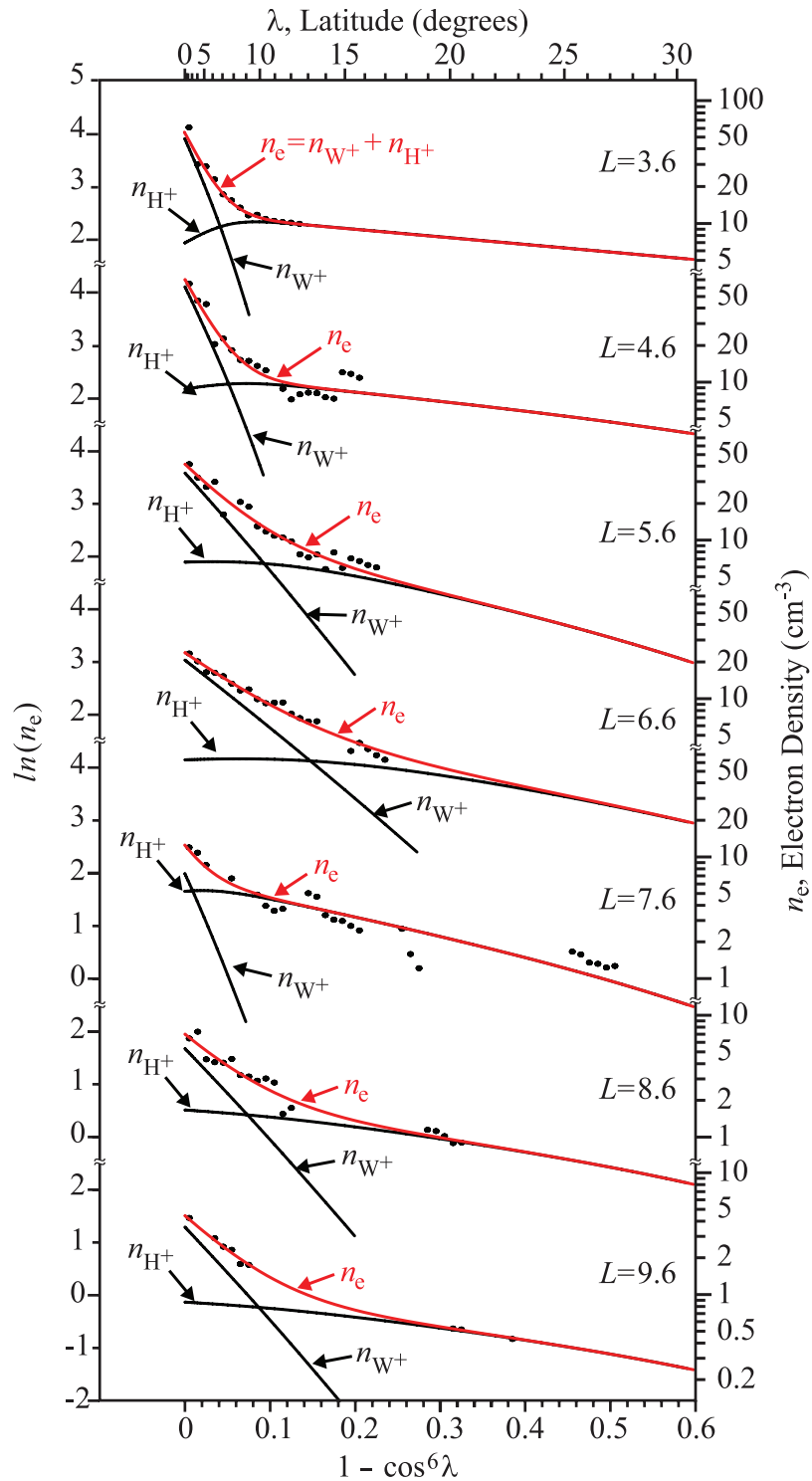


**Figure 11.** A multipanel plot in the same format as that of Figure 10, showing the diffusive equilibrium model fit to the RPWS electron densities for seven  $L$ -shell bins from 3.6 to 9.6. At low  $L$  values, the ambipolar term strongly suppresses the hydrogen ion density at the equator, while the mirror term adjusts the density fit to match the low densities at higher latitudes.

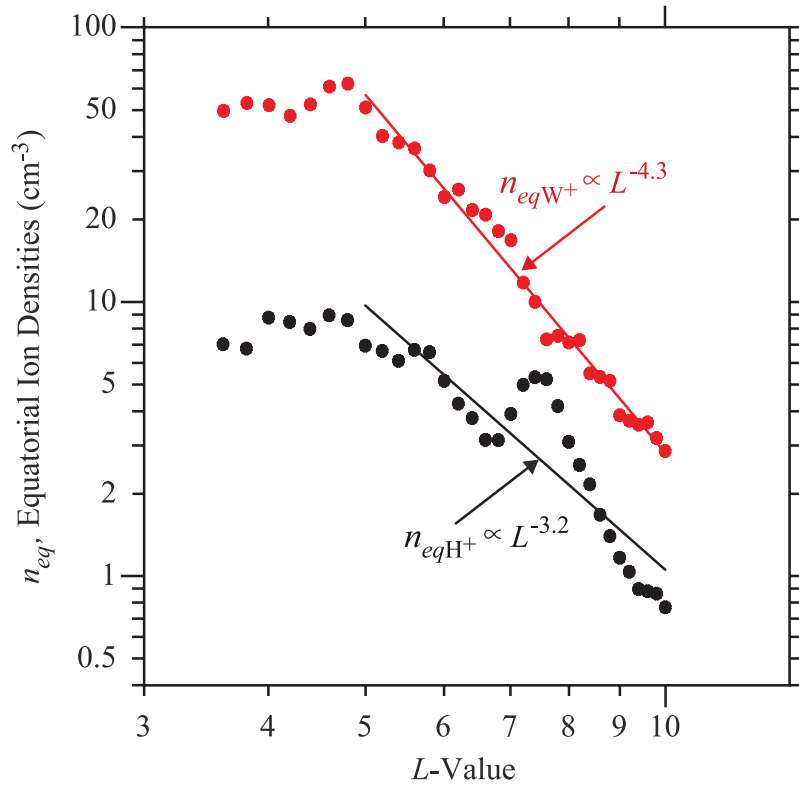


**Figure 12.** A plot of the ion equatorial densities derived from the least squares fit to the RPWS electron densities in four-parameter space for  $3.6 \leq L \leq 10.0$ . At low  $L$  values, the ions increase slightly, reaching a broad peak outside  $L = 4$ , the result of the ionization of water group neutrals emitted by the moon Enceladus. Beyond  $L = 5$ , both ion species diffuse radially outward from Saturn with an inverse  $L$ -shell dependence of  $n_{eqW^+} \propto L^{-4.3}$  and  $n_{eqH^+} \propto L^{-3.2}$ .

for the ion and electron densities from field-aligned force balance equations similar in form to equation (1). The  $\rho, z$  extent of the constant density contours for the electrons and ions is similar in both models. Particularly striking is the off-equator hydrogen ion density peak at  $10 \text{ cm}^{-3}$  just inside  $\rho = 4 R_S$ , a feature visible in Figure 14 and in the contour map of *Sittler et al.* [2008, Figure 5].

## 7. Summary

[28] A diffusive equilibrium model is used to describe the distribution of plasma in Saturn's inner magnetosphere. The model provides a good fit to the electron densities measured by the RPWS instrument on Cassini over a 39-month period from 30 June 2004 through 30 September 2007. The measurements span a range of latitudes from the equator to  $35^\circ$  and  $L$  values from 3.6 to 10. The model yields information on the ion scale heights and the equatorial densities of the water group and the hydrogen ions, the two major ion components of the plasma in this part of Saturn's magnetosphere. For both species, the equatorial density profile has a broad peak inside  $L = 5$ , which can be attributed to the ionization of neutral gases being emitted from Enceladus' southern polar region. The equatorial density profile for the water group ions peaks at  $62 \text{ cm}^{-3}$  at  $L = 4.8$  and the equatorial density profile for the hydrogen ions peaks at  $9 \text{ cm}^{-3}$  at  $L = 4.6$ . Beyond  $L = 5$ , the equatorial density profiles for both ion species show an inverse  $L$ -value

dependence of  $n_{eqW^+} \propto L^{-4.3}$  and  $n_{eqH^+} \propto L^{-3.2}$ . Although the scale height for the water group ions is an order of magnitude smaller than the hydrogen ion scale height, the scale heights for both ion species show a similar, strong positive  $L$ -value dependence of  $H_{W^+} \propto L^{1.5}$  and  $H_{H^+} \propto L^{1.4}$ . Corresponding ion temperatures derived from the ion scale heights range from several eV at  $L = 3.6$  to  $\sim 100 \text{ eV}$  at  $L = 10$ .

[29] Density contour maps derived from these equatorial densities and ion scale heights for the water group ions, the hydrogen ions and the electrons have been found to be consistent with earlier density contour maps [*Richardson and Jurac*, 2004; *Sittler et al.*, 2008]. The contours of constant density show the plasma diffusing radially outward from the planet and expanding away from the equatorial plane. The hydrogen density contours clearly show the effect of the ambipolar electric field on the lighter ions close to Saturn, with an off-equator hydrogen ion density peak at  $9 \text{ cm}^{-3}$  for  $3.6 \leq \rho \leq 4 R_S$ , a feature visible in Figure 14 and in the contour map of *Sittler et al.* [2008, Figure 5] just inside  $4 R_S$ . However, unlike the earlier density contour maps, the ambipolar effect is not seen in the hydrogen ion density contours beyond  $5 R_S$  in the diffusive equilibrium model, owing to the opposing effect of the increasingly strong mirror force in this region.

[30] The diffusive equilibrium model is based on several assumptions designed to simplify the analysis. To give a smooth functional representation for the electron temperature input, we have averaged and smoothed three indepen-

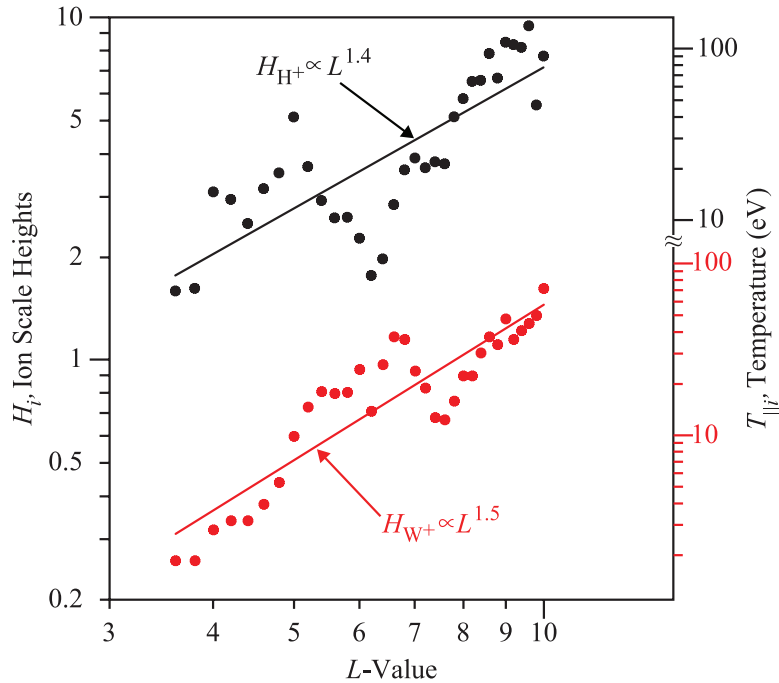


**Figure 13.** A plot of the ion scale heights derived from the diffusive equilibrium model fit to the RPWS electron densities for  $3.6 \leq L \leq 10.0$ . The scale heights for both ion species increase systematically and rapidly with increasing  $L$  value, with the water group ion scale height varying as  $H_{W^+} \propto L^{1.5}$  and the hydrogen ion scale height varying as  $H_{H^+} \propto L^{1.4}$ , consistent with a latitudinally expanding ion torus. The corresponding ion temperatures  $T_{\parallel i}$ , derived from equation (3) and shown on the right vertical axis, range from several eV at  $L = 4$  to  $\sim 100$  eV at  $L = 10$ .

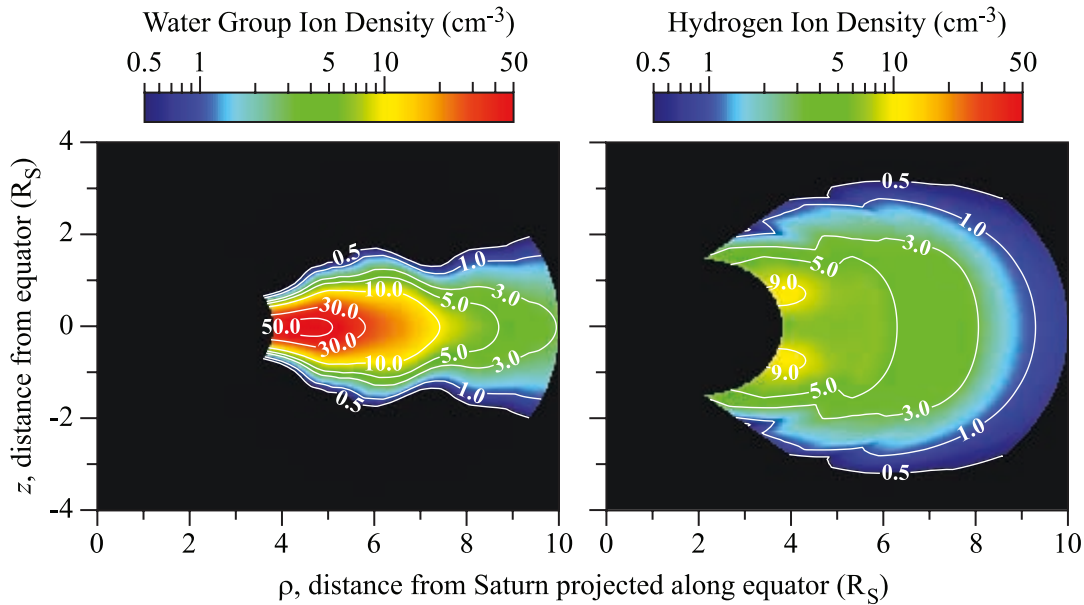


**Figure 14.** Contour plots of the water group and hydrogen ion densities in Saturn's inner magnetosphere constructed from the diffusive equilibrium model, where  $z$  is the distance above/below the equatorial plane and  $\rho$  is the perpendicular distance from Saturn's spin axis. The contour plots are constructed assuming azimuthal symmetry about the spin axis and mirror symmetry about the equator. The contours of constant density clearly show that the heavier ions are closely confined to the equatorial plane, with the highest densities ( $n_{W^+} \geq 30 \text{ cm}^{-3}$ ) found for  $L \leq 6$  and  $|z| \leq 0.5 R_S$ . Inside  $L \approx 5$  the contours of constant density clearly show the hydrogen ion population expanding away from the equatorial plane under the influence of a strong ambipolar force. Outside  $L \approx 5$ , the increasing strength of the mirror force opposes the ambipolar effect, creating a radially diffusive plasma distribution.

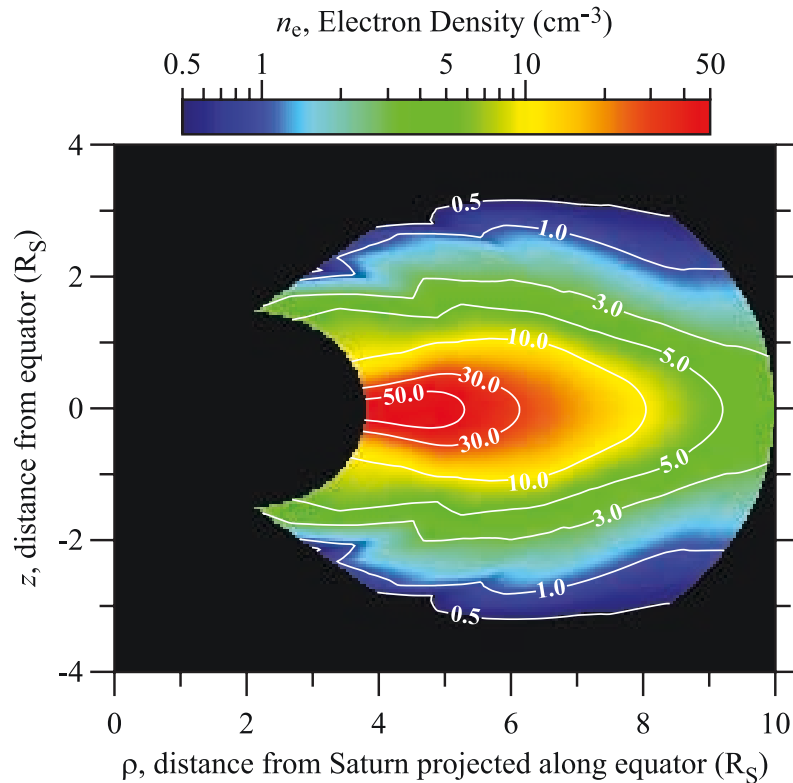


**Figure 15.** Contour plot of the electron densities in Saturn’s inner magnetosphere derived from the charge neutrality condition. The contour map shows that the electrons in Saturn’s magnetosphere diffuse radially outward from the planet with the higher densities located near the equatorial plane inside  $L = 7$ .

dent sets of electron temperature measurements from the CAPS instrument and from the RPWS using quasi-thermal noise spectroscopy and the Langmuir probe (Figure 2). Since the three sets of temperature measurements are consistent within a factor of 2 and show a systematic and smooth increase in the electron temperature with increasing  $L$  value, we have strong confidence in the temperatures we have used. However, a possible latitudinal dependence for the electron temperature has not yet been investigated. The electron temperatures derived from Cassini measurements [Moncuquet *et al.*, 2005; Schippers *et al.*, 2008; Wahlund *et al.*, 2005] show a steady increase with increasing  $L$  value, consistent with temperatures derived from the Voyager measurements [Sittler *et al.*, 1983]. However, a possible latitudinal dependence may also be present in the temperature profiles for measurements obtained during the Cassini orbit insertion [Moncuquet *et al.*, 2005; Wahlund *et al.*, 2005] and the Voyager flybys [Sittler *et al.*, 1983] when the spacecraft were in high inclination orbits. A more thorough study of the effect of a latitudinally dependent electron temperature on the diffusive equilibrium density model will be the subject of a future study.

[31] Limited data availability necessitated several major assumptions for the ion anisotropies. The anisotropy inputs are shown to be critically important in the density fit and a precise determination of these parameters is currently available only at equatorial latitudes beyond  $L = 5.5$ . Extrapolating the anisotropies back to  $L = 3.6$  is only a rough estimate. Also, the assumption that the ion anisotropies measured at the equator remain constant along a field

line may not be valid. There are large variations in the ion anisotropies as a function of  $L$  shell in both the Cassini measurements (see Figure 3) and the Voyager measurements [Maurice *et al.*, 1996; Richardson and Eviatar, 1988]. Large variations in the ion anisotropy have little effect on the water group ions (see Figure 5). But, if the hydrogen ion anisotropy is found to decrease with increasing latitude, it can have a significant effect on a successful fit to the measured densities (see Figure 6). More anisotropy measurements inside  $L = 5$  and at higher latitudes are necessary to improve the density fit at higher latitudes and the validity of the hydrogen ion distribution derived from the diffusive equilibrium model.

[32] Although the diffusive equilibrium model consistently yields well-defined minima in  $(n_{eqW^+} - H_{W^+})$  space for the water group ions (see Figure 10a), the limited and inconsistent distribution of density data at high latitudes across the  $L$ -shell range makes it difficult to anchor the fit at the high-latitude end of the range and obtain precise density minima for the hydrogen ions, which dominate the plasma in this region. While the equatorial density of the hydrogen ions can be determined with some precision, the hydrogen ion density minima in chi-square occasionally resembles a “trough” and, for these  $L$ -shell bins, the hydrogen ion scale height is not well-defined. The ion equatorial densities and scale heights shown in Figures 12 and 13 represent solutions that are consistent with the distribution of the plasma density measurements. Improving the fit at the high-latitude end of the distribution and the subsequent derivation of the hydrogen ion scale height will require more density



measurements above  $20^\circ$  for all  $L$  values in the inner magnetosphere.

[33] Finally, using the diffusive equilibrium model to fit the density measurements at  $L < 3.6$  has not been entirely successful. Because of Cassini orbit constraints, the density measurements in this region span a limited latitudinal range near the equatorial plane, making it difficult to anchor the density fit at higher latitudes and derive reasonable values for the ion scale heights. The other difficulty is the wide scatter in the density measurements for  $L \leq 4$ , due to the longitude-dependence of the electron density [Gurnett *et al.*, 2007]. It will be the work of a future study to include a longitudinal factor in the diffusive equilibrium model.

### Appendix A: An Analytical Solution of the Diffusive Equilibrium Equations

[34] To derive an analytic solution to the diffusive equilibrium equations we start with the magnetic field-aligned force balance equation (1):

$$\begin{aligned} \frac{\partial P_{\parallel}}{\partial s} = & (P_{\parallel} - P_{\perp}) \frac{1}{B} \frac{\partial B}{\partial s} + n_i m_i \frac{\partial}{\partial s} \left( \frac{1}{2} \Omega^2 \rho^2 \right) \\ & + n_i \frac{\partial}{\partial s} \left( \frac{GM_S m_i}{r} \right) - n_i q_i \frac{\partial \Phi}{\partial s}, \end{aligned} \quad (A1)$$

where  $P_{\parallel} = n_i \kappa T_{\parallel}$  and  $P_{\perp} = n_i \kappa T_{\perp}$  are the parallel and perpendicular pressures and  $T_{\parallel}$  and  $T_{\perp}$  are the parallel and perpendicular temperatures. It is convenient to define the anisotropy as  $A_i = (T_{\perp}/T_{\parallel}) - 1$ . Using this definition for the anisotropy the force equation can be written as

$$\begin{aligned} \kappa T_{\parallel} \frac{\partial n_i}{\partial s} = & -n_i \kappa T_{\parallel} A_i \frac{1}{B} \frac{\partial B}{\partial s} + n_i m_i \frac{\partial}{\partial s} \left( \frac{1}{2} \Omega^2 \rho^2 \right) \\ & + n_i \frac{\partial}{\partial s} \left( \frac{GM_S m_i}{r} \right) - n_i q_i \frac{\partial \Phi}{\partial s}. \end{aligned} \quad (A2)$$

To further simplify this equation, we divide by  $n_i$  and  $\kappa T_{\parallel}$  and rewrite  $\frac{1}{n_i} \frac{\partial n_i}{\partial s}$  as  $\frac{\partial}{\partial s} (\ln n_i)$ . Note that  $\Omega$ ,  $G$ ,  $M_S$ ,  $m_i$ , and  $q_i$  are constants. The force balance equation then becomes

$$\begin{aligned} \frac{\partial}{\partial s} (\ln n_i) = & -A_i \frac{1}{B} \frac{\partial B}{\partial s} + \frac{1}{2} \frac{m_i \Omega^2}{\kappa T_{\parallel}} \frac{\partial}{\partial s} (\rho^2) \\ & + \frac{GM_S m_i}{\kappa T_{\parallel}} \frac{\partial}{\partial s} \left( \frac{1}{r} \right) - \frac{q_i}{\kappa T_{\parallel}} \frac{\partial \Phi}{\partial s}. \end{aligned} \quad (A3)$$

Next we integrate equation (A3) along the magnetic field line. Note that all of the terms, except the first term on the right (the mirror term), are exact differentials. Equation (A3) can then be integrated along the magnetic field line from the equator,  $s = 0$ , to an arbitrary point  $s$  along the magnetic field line to give

$$[\ln n_i]_0^s = - \int_0^s A_i \frac{dB}{B} + \frac{1}{2} \frac{m_i \Omega^2}{\kappa T_{\parallel}} [\rho^2]_0^s + \frac{GM_S m_i}{\kappa T_{\parallel}} \left[ \frac{1}{r} \right]_0^s - \frac{q_i}{\kappa T_{\parallel}} [\Phi]_0^s. \quad (A4)$$

At the equator, where  $\rho = r = R_0$ , we set the electrostatic potential  $\Phi$  to zero and define  $n_{ieq}$  to be the equatorial density. Evaluating the limits in equation (A4) then gives

$$\begin{aligned} \ln \frac{n_i}{n_{ieq}} = & - \int_0^s A_i \frac{dB}{B} - \frac{1}{2} \frac{m_i \Omega^2}{\kappa T_{\parallel}} [R_0^2 - \rho^2] \\ & - \frac{GM_S m_i}{\kappa T_{\parallel}} \left[ \frac{1}{R_0} - \frac{1}{r} \right] - \frac{q_i}{\kappa T_{\parallel}} \Phi. \end{aligned} \quad (A5)$$

For a dipole field, the radius to the magnetic field line is given by  $r = R_0 \cos^2 \lambda$ . Substituting this relation into equation (A5) and introducing cylindrical coordinate,  $\rho = r \cos \lambda$ , then gives

$$\begin{aligned} \ln \frac{n_i}{n_{ieq}} = & - \int_0^s A_i \frac{dB}{B} - \frac{1}{2} \frac{m_i \Omega^2 R_0^2}{\kappa T_{\parallel}} [1 - \cos^6 \lambda] \\ & - \frac{GM_S m_i}{\kappa T_{\parallel} R_0} \left[ 1 - \frac{1}{\cos^2 \lambda} \right] - \frac{q_i}{\kappa T_{\parallel}} \Phi. \end{aligned} \quad (A6)$$

Using the definition for  $L$  value from McIlwain [1961]  $L = R_0/R_S$ , where  $R_S$  is the radius of Saturn, and making the substitution  $[1 - (1/\cos^2 \lambda)] = -\tan^2 \lambda$ , equation (A6) becomes

$$\begin{aligned} \ln \frac{n_i}{n_{ieq}} = & - \int_0^s A_i \frac{dB}{B} - \frac{1}{2} \frac{m_i \Omega^2 R_S^2}{\kappa T_{\parallel}} L^2 (1 - \cos^6 \lambda) \\ & + \frac{GM_S m_i}{\kappa T_{\parallel} R_S} \frac{\tan^2 \lambda}{L} - \frac{q_i}{\kappa T_{\parallel}} \Phi. \end{aligned} \quad (A7)$$

Next we proceed to simplify each of the terms on the right-hand side of equation (A7). In the absence of detailed information on the pitch angle distribution of the particles, we must make some assumption about how the anisotropy varies along the magnetic field line. For simplicity we assume that the anisotropy  $A_i$  is constant along the magnetic field line. This assumption is expected to be valid near the equator, but may fail at higher latitudes. With this simplifying assumption the mirror term can then be written as

$$\int_0^s A_i \frac{dB}{B} = A_i \int_0^s \frac{dB}{B} = A_i [\ln B]_0^s = A_i \ln \frac{B}{B_0}. \quad (A8)$$

Using the equation for a dipole magnetic field [Jackson, 1962], it is easy to show that

$$B = \frac{B_S R_S^3}{r^3} [4 \sin^2 \lambda + \cos^2 \lambda]^{1/2} = \frac{B_S R_S^3}{r^3} [1 + 3 \sin^2 \lambda]^{1/2}, \quad (A9)$$

where  $B_S$  is the equatorial magnetic field strength at the surface of Saturn.

[35] Substituting  $r = R_0 \cos^2 \lambda$ , and  $B_0 = B_S \left(\frac{R_S}{r}\right)^3$  for the magnetic field at any point along the equator, the mirror term can now be written as a function of latitude only:

$$A_i \ln \frac{B}{B_0} = A_i \ln \left[ \frac{1}{\cos^6 \lambda} (1 + 3 \sin^2 \lambda)^{1/2} \right]. \quad (A10)$$

By defining a dimensionless scale height  $H_i$ , which is the scale height divided by the radius of Saturn [Persoon et al., 2006a], the centrifugal term can be simplified using

$$\frac{1}{2} \frac{m_i \Omega^2 R_S^2}{\kappa T_{\parallel}} = \frac{1}{3} \frac{1}{H_i^2}. \quad (\text{A11})$$

Note that the scale height defined above is related to the temperature:

$$\kappa T_{\parallel} = \frac{3}{2} m_i \Omega^2 R_S^2 H_i^2. \quad (\text{A12})$$

To simplify the gravitational and ambipolar terms, we define three constants:

$$\alpha = \frac{GM_S m_i H_i^2}{\kappa T_{\parallel} R_S} = \frac{2GM_S}{3\Omega^2 R_S^3}, \quad \beta_i = \frac{q_i H_i^2}{\kappa T_{\parallel}} = \frac{2q_i}{3m_i \Omega^2 R_S^3}, \quad (\text{A13})$$

where  $\alpha$  is a dimensionless constant and  $\beta_i$  is a constant with units of  $V^{-1}$ .

[36] Using the numerical constants  $G = 6.673 \times 10^{-11} \text{ Nm}^2/\text{kg}^2$ ,  $M_S = 5.688 \times 10^{26} \text{ kg}$ ,  $\Omega = 1.638 \times 10^{-4} \text{ rad/s}$  for a planetary rotation period of 10 h 39 m 24 s [Desch and Kaiser, 1981],  $q_i = q_{H^+} = e = 1.602 \times 10^{-19} \text{ C}$ ,  $m_{H^+} = 1.6725 \times 10^{-27} \text{ kg}$  (hydrogen ions), and  $m_{W^+} = 18 m_{H^+}$  (water group ions), the three constants become  $\alpha = 4.308$ ,  $\beta_{H^+} = 0.6550 \text{ V}^{-1}$ , and  $\beta_{W^+} = 0.0364 \text{ V}^{-1}$ . Using these constants in the gravitational and ambipolar terms and substituting equations (A10) and (A12) in the centrifugal and mirror terms, the full force diffusive equilibrium equation can now be written as a function of density, plasma scale height,  $L$  value, and latitude:

$$\ln \frac{n_i}{n_{ieq}} = -A_i \ln \left[ \frac{1}{\cos^6 \lambda} (1 + 3 \sin^2 \lambda)^{1/2} \right] - \frac{1}{3} \frac{L^2}{H_i^2} (1 - \cos^6 \lambda) + \frac{\alpha \tan^2 \lambda}{L H_i^2} - \frac{\beta_i}{H_i^2} \Phi. \quad (\text{A14})$$

The final form of the equation for the density of the  $i$ th species now becomes

$$n_i = n_{ieq} \exp \left[ -A_i \ln \left[ \frac{1}{\cos^6 \lambda} (1 + 3 \sin^2 \lambda)^{1/2} \right] - \frac{1}{3} \frac{L^2}{H_i^2} (1 - \cos^6 \lambda) + \frac{\alpha \tan^2 \lambda}{L H_i^2} - \frac{\beta_i}{H_i^2} \Phi \right]. \quad (\text{A15})$$

[37] **Acknowledgments.** The Cassini radio and plasma wave research at the University of Iowa is supported by NASA through JPL contract 1279973. We thank the CAPS and ELS operations teams at SwRI and MSSL, the ion mass spectrometer team at Los Alamos under the auspices of the U.S. DOE, STFC for financial support in the U.K., and NASA/JPL contract 1243218 for financial support of the CAPS investigation.

[38] Wolfgang Baumjohann thanks James Burch and another reviewer for their assistance in evaluating this paper.

## References

Bevington, P. R., and D. K. Robinson (1992), *Data Reduction and Error Analysis for the Physical Sciences*, p. 67, McGraw-Hill, New York.

Bridge, H. S., et al. (1981), Plasma observations near Saturn: Initial results from Voyager 1, *Science*, *212*, 217–224, doi:10.1126/science.212.4491.217.

Bridge, H. S., et al. (1982), Plasma observations near Saturn: Initial results from Voyager 2, *Science*, *215*, 563–570, doi:10.1126/science.215.4532.563.

Connery, J. E. P., L. Davis Jr., and D. L. Chenette (1984), Magnetic field models, in *Saturn*, edited by T. Gehrels and M. S. Matthews, pp. 354–377, Univ. of Ariz. Press, Tucson.

Desch, M. D., and M. L. Kaiser (1981), Voyager measurement of the rotation period of Saturn's magnetic field, *Geophys. Res. Lett.*, *8*, 253–256, doi:10.1029/GL008i003p00253.

Frank, L. A., B. G. Burek, K. L. Ackerson, J. H. Wolfe, and J. D. Mihalov (1980), Plasma in Saturn's magnetosphere, *J. Geophys. Res.*, *85*, 5695–5708, doi:10.1029/JA085iA11p05695.

Gledhill, J. A. (1967), Magnetosphere of Jupiter, *Nature*, *214*, 155–156, doi:10.1038/214155a0.

Gurnett, D. A., et al. (2004), The Cassini radio and plasma wave investigation, *Space Sci. Rev.*, *114*, 395–463.

Gurnett, D. A., A. M. Persoon, W. S. Kurth, J. B. Groene, T. F. Averkamp, M. K. Dougherty, and D. J. Southwood (2007), The variable rotation period of the inner region of Saturn's plasma disk, *Science*, *316*, 442–445, doi:10.1126/science.1138562.

Hill, T. W., and F. C. Michel (1976), Heavy ions from the Galilean satellites and the centrifugal distortion of the Jovian magnetosphere, *J. Geophys. Res.*, *81*, 4561–4565, doi:10.1029/JA081i025p04561.

Jackson, J. D. (1962), *Classical Electrodynamics*, p. 72, John Wiley, New York.

Kaiser, M. L., M. D. Desch, W. S. Kurth, A. Lecacheux, F. Genova, B. M. Pedersen, and D. R. Evans (1984), Saturn as a radio source, in *Saturn*, edited by T. Gehrels and M. S. Matthews, pp. 378–415, Univ. of Ariz. Press, Tucson.

Lewis, G. R., N. Andre, C. S. Arridge, A. J. Coates, L. K. Gilbert, D. R. Linder, and A. M. Rymer (2008), Derivation of density and temperature from the Cassini-Huygens CAPS electron spectrometer, *Planet. Space Sci.*, *56*, 901–912, doi:10.1016/j.pss.2007.12.017.

Matson, D. L., L. J. Spilker, and J.-P. Lebreton (2002), The Cassini/Huygens mission to the Saturnian system, *Space Sci. Rev.*, *104*, 1–58, doi:10.1023/A:1023609211620.

Maurice, S., E. C. Sittler, J. F. Cooper, B. H. Mauk, M. Blanc, and R. S. Selesnick (1996), Comprehensive analysis of electron observations at Saturn: Voyager 1 and 2, *J. Geophys. Res.*, *101*, 15,211–15,232, doi:10.1029/96JA00765.

McIlwain, C. E. (1961), Coordinates for mapping the distribution of magnetically trapped particles, *J. Geophys. Res.*, *66*, 3681–3691, doi:10.1029/JZ066i011p03681.

Moncuquet, M., A. Lecacheux, N. Meyer-Vernet, B. Cecconi, and W. S. Kurth (2005), Quasi thermal noise spectroscopy in the inner magnetosphere of Saturn with Cassini/RPWS: Electron temperatures and density, *Geophys. Res. Lett.*, *32*, L20S02, doi:10.1029/2005GL022508.

Persoon, A. M., D. A. Gurnett, W. S. Kurth, G. B. Hospodarsky, J. B. Groene, P. Canu, and M. K. Dougherty (2005), Equatorial electron density measurements in Saturn's inner magnetosphere, *Geophys. Res. Lett.*, *32*, L23105, doi:10.1029/2005GL024294.

Persoon, A. M., D. A. Gurnett, W. S. Kurth, and J. B. Groene (2006a), A simple scale height model of the electron density in Saturn's plasma disk, *Geophys. Res. Lett.*, *33*, L18106, doi:10.1029/2006GL027090.

Persoon, A. M., D. A. Gurnett, W. S. Kurth, G. B. Hospodarsky, J. B. Groene, P. Canu, and M. K. Dougherty (2006b), An electron density model for Saturn's inner magnetosphere, in *Planetary Radio Emissions VI*, edited by H. O. Rucker, W. S. Kurth, and G. Mann, pp. 81–91, Austrian Acad. of Sci. Press, Vienna.

Richardson, J. D. (1995), An extended plasma model for Saturn, *Geophys. Res. Lett.*, *22*, 1177–1180, doi:10.1029/95GL01018.

Richardson, J. D. (1998), Thermal plasma and neutral gas in Saturn's magnetosphere, *Rev. Geophys.*, *36*, 501–524, doi:10.1029/98RG01691.

Richardson, J. D., and A. Eviatar (1988), Observational and theoretical evidence for anisotropies in Saturn's magnetosphere, *J. Geophys. Res.*, *93*, 7297–7306, doi:10.1029/JA093iA07p07297.

Richardson, J. D., and S. Jurac (2004), A self-consistent model of plasma and neutrals at Saturn: The ion tori, *Geophys. Res. Lett.*, *31*, L24803, doi:10.1029/2004GL020959.

Richardson, J. D., and E. C. Sittler Jr. (1990), A plasma density model for Saturn based on Voyager observations, *J. Geophys. Res.*, *95*, 12019–12031, doi:10.1029/JA095iA08p12019.

Rymer, A. M., et al. (2007), Electron sources in Saturn's magnetosphere, *J. Geophys. Res.*, *112*, A02201, doi:10.1029/2006JA012017.

Scarf, F. L., L. A. Frank, D. A. Gurnett, L. J. Lanzerotti, A. Lazarus, and E. J. Sittler Jr. (1984), Measurements of plasma, plasma waves, and suprathermal charged particles in Saturn's inner magnetosphere, in *Saturn*, edited by T. Gehrels and M. S. Matthews, pp. 318–353, Univ. of Ariz. Press, Tucson.

Schippers, P., et al. (2008), Multi-instrument analysis of electron populations in Saturn's magnetosphere, *J. Geophys. Res.*, *113*, A07208, doi:10.1029/2008JA013098.

- Sittler, E. C., Jr., K. W. Ogilvie, and J. D. Scudder (1983), Survey of low-energy plasma electrons in Saturn's magnetosphere, *J. Geophys. Res.*, *88*, 8847–8870, doi:10.1029/JA088iA11p08847.
- Sittler, E. C., Jr., et al. (2006), Cassini observations of Saturn's inner plasmasphere: Saturn orbit insertion results, *Planet. Space Sci.*, *54*, 1197–1210, doi:10.1016/j.pss.2006.05.038.
- Sittler, E. C., Jr., et al. (2008), Ion and neutral sources and sinks within Saturn's inner magnetosphere: Cassini results, *Planet. Space Sci.*, *56*, 3–18, doi:10.1016/j.pss.2007.06.006.
- Tokar, R. L., et al. (2008), Cassini detection of water-group pick-up ions in the Enceladus torus, *Geophys. Res. Lett.*, *35*, L14202, doi:10.1029/2008GL034749.
- Trainor, J. H., F. B. McDonald, and A. W. Schardt (1980), Observations of energetic ions and electrons in Saturn's magnetosphere, *Science*, *207*, 421–424, doi:10.1126/science.207.4429.421.
- Wahlund, J.-E., et al. (2005), The inner magnetosphere of Saturn: Cassini RPWS cold plasma results from the first encounter, *Geophys. Res. Lett.*, *32*, L20S09, doi:10.1029/2005GL022699.
- Wilson, R. J., R. L. Tokar, M. G. Henderson, T. W. Hill, M. F. Thomsen, and D. H. Pontius (2008), Cassini plasma spectrometer thermal ion measurements in Saturn's inner magnetosphere, *J. Geophys. Res.*, *113*, A12218, doi:10.1029/2008JA013486.
- Wolfe, J. H., J. D. Mihalov, H. R. Collard, D. D. McKibbin, L. A. Frank, and D. S. Intriligator (1980), Preliminary results on the plasma environment of Saturn from the Pioneer 11 plasma analyzer experiment, *Science*, *207*, 403–407, doi:10.1126/science.207.4429.403.
- Young, D. T., et al. (2005), Composition and dynamics of plasma in Saturn's magnetosphere, *Science*, *307*, 1262–1266, doi:10.1126/science.1106151.
- 
- A. J. Coates and G. R. Lewis, Mullard Space Science Laboratory, University College London, Dorking RH5 6NT, UK.
- J. B. Faden, J. B. Groene, D. A. Gurnett, W. S. Kurth, and A. M. Persoon, Department of Physics and Astronomy, University of Iowa, Iowa City, IA 52242-1479, USA. (ann-persoon@uiowa.edu)
- M. Moncuquet, Laboratoire d'Etudes Spatiales et Instrumentation en Astrophysique, Observatoire de Paris, F-92195 Meudon, France.
- O. Santolik, Institute of Atmospheric Physics, 14131 Prague 4, Czech Republic.
- R. L. Tokar and R. J. Wilson, Space and Atmospheric Science Group, Los Alamos National Laboratory, Los Alamos, NM 87545, USA.
- J.-E. Wahlund, Swedish Institute of Space Physics, SE-751 21 Uppsala, Sweden.